

A Low Cost Relativistic Algebraic Diagrammatic Construction Method Based on Cholesky Decomposition and Frozen Natural Spinors for Electronic Ionization, Attachment and Excitation Energy Problem

Sudipta Chakraborty,[†] Kamal Majee,[†] and Achintya Kumar Dutta^{*,†,‡}

[†]*Department of Chemistry, Indian Institute of Technology Bombay, Mumbai 400076, India*

[‡]*Department of Inorganic Chemistry, Faculty of Natural Sciences, Comenius University, Bratislava Ilkovičova 6, Mlynská dolina 842 15 Bratislava, Slovakia*

E-mail: achintya@chem.iitb.ac.in

Abstract

We present an efficient relativistic implementation of the algebraic diagrammatic construction (ADC) theory up to third order, incorporating Cholesky decomposition (CD) and frozen natural spinor (FNS) techniques to address electronic ionization, attachment, and excitation problems in heavy-element systems. The exact two-component atomic mean-field (X2CAMF) Hamiltonian has been employed to balance accuracy with computational efficiency, and a state-specific frozen natural spinor (SS-FNS) extension has been developed to improve excited-state descriptions. The present implementation accurately reproduces canonical four-component third-order ADC results while significantly lowering computational demands. The efficiency and performance of the present implementation are demonstrated through calculations on larger

systems, with the largest system successfully treated comprising more than 2600 basis functions.

1 Introduction

The accurate and efficient simulation of electronic excitation, ionization, and electron attachment processes remains a cornerstone for understanding a wide range of chemical and physical processes, such as photochemical reactions, electronic spectroscopy, charge transfer phenomena, and photoionization.[1] Numerous methods have been developed for evaluating ionized, electron-attached, and excited-state energies, which can be broadly classified into two categories. The first, known as “ Δ - based methods,” involves performing two separate total energy calculations, one for the ground state and another for the target state, and subsequently taking their difference to obtain the desired energy. The other approach is the “direct energy-difference method,” which requires only a single calculation from which the excitation, ionization, or electron attachment energies are directly obtained as eigenvalues of an effective secular Hamiltonian. The former approach often suffers from issues like symmetry breaking and variational collapse of the wave function, which can compromise the reliability of the computed energy differences. In addition to these challenges, it also lacks access to important transition properties, including spectroscopic amplitudes or intensities. In contrast, the latter approach is generally free from these problems and is therefore more commonly used in modern electronic structure calculations.

The equation-of-motion coupled cluster (EOM-CC)[2–5] method has become one of the most widely used direct difference-based wavefunction methods for computing excitation energy (EE), electron attachment (EA), and ionization potential (IP) energy. The linear-response coupled cluster (LR-CC)[6, 7] method gives identical excitation energies, although it is formulated from a different theoretical perspective than the EOM-CC approaches. However, in both cases, the non-Hermitian nature of the effective Hamiltonian within a basis of the

biorthogonal CC framework makes the eigenvalue problems prone to complex solutions. [8] Moreover, the computation of transition properties in the standard CC method is challenging, as it requires the determination of both left and right eigenvectors. The unitary coupled cluster (UCC) approach offers a Hermitian formulation of CC methods and helps to address these challenges.[9, 10] However, the non-termination Baker-Campbell-Hausdorff (BCH) expansion of the similarity-transformed Hamiltonian poses significant challenges for practical implementation of the UCC method. To address this issue, commutator-based truncation schemes within UCC theory have garnered considerable attention due to their implications in quantum computing. However, they are shown to be advantageous even on classical computers.[11, 12]

In contrast of these iterative nature of CC- based method the Algebraic Diagrammatic Construction (ADC)[13–19], scheme has attracted considerable attention due to its low-cost, non-iterative treatment of the ground state wave-function based on Møller–Plesset perturbation theory (MPn), as well as its Hermitian formulation, which provides distinct advantages in the calculation of excited state properties. The ADC method was first developed using the propagator formalism[16, 20]. The propagator-based ADC methods were successfully applied to compute electron-ionization and attachment spectra[21–24]. In modern implementations of ADC, the intermediate-state representation (ISR) has emerged as the preferred approach, largely due to its transparent formalism and its provision of direct access to the excited-state wavefunction.[15] An extension of the fourth-order ADC (ADC(4)) scheme within the ISR formalism for EE, IP, and EA has been proposed by Dreuw and co-workers.[25, 26] In recent years, ADC methods have been extensively employed for energy and property calculations, particularly in lighter elements[13, 18, 20, 26–31]. For atoms and molecules containing heavy elements, the inclusion of relativistic effects becomes essential. One of the most straightforward ways of introducing relativistic effects in quantum chemical calculations is to use a four-component Dirac Coulomb Hamiltonian.[32] Pernpointner et al. have implemented the second-order and the extended second-order versions of ADC methods based on the

four-component relativistic Hamiltonian, demonstrating its capability to compute excitation energies and transition dipole moments. [33, 34] In addition, non-Dyson-based second and third-order ADC schemes have been developed within the relativistic framework to compute valence ionization energies and investigate the electron decay process[35, 35–37]. Although the second-order ADC (ADC(2)) can give qualitative agreement, it typically lacks quantitative accuracy. To achieve more reliable results, it is necessary to go beyond second-order and include at least third-order contributions in the perturbative expansion. To address this, we have recently developed a four-component(4c) ADC(3) method for calculating IP, EA, EE, and excited state properties of atoms and molecules containing heavy elements[38]. However, performing 4c-ADC(3) calculations remains a significant challenge due to their extremely high computational cost, often up to 32 times greater than that of a non-relativistic method[32]. As a result, such calculations are typically limited to atoms and small molecules using a moderate-sized basis set. To mitigate this limitation, numerous approaches have been developed in the literature to lower the computational cost in the relativistic electronic structure calculation. One of the most effective strategies is the use of two-component relativistic theories[32, 39–44]. Among the various flavours of two-component methods available, the exact two-component (X2C) theory based on atomic mean field (AMF) spin-orbit integrals (X2CAMF) has emerged as one of the most attractive ones[45–47]. It can be further combined with the cholesky decomposition(CD) treatment of the integrals[48–50]. Sokolov and co-workers[51] have recently reported a single-reference and multi-reference ADC method for ionization and electron attachment problems based on a one-electron variant of the X2C method (X2C-1e). In addition to the simplification offered by the two-component framework, leveraging massively parallel programs can accelerate the floating-point operations of relativistic electron correlation method.[52] Alternatively, one can use a more compact set of spinor space in the form of frozen natural spinors (FNS), which allows one to perform effective truncation of the virtual space with systematic controllable accuracy. The FNS are generally constructed from MP2 calculations, and the efficiency of the MP2-based FNS

has been demonstrated in relativistic four-component ground-state coupled cluster (CC)[53] and unitary coupled cluster (UCC)[11] calculations. This approach has also been extended to core and valence ionization problems[54] using the equation of motion coupled cluster approach(EOM-CC). Gomes and co-workers[55] have reported a similar natural spinor-based strategy for the ground-state CC method. To further reduce the computational cost, the FNS method can be combined with the CD decomposition-based X2CAMF-CC method[56]. Gomes and coworkers[55] have demonstrated that, in contrast to ground state energy calculations, standard MP2-based natural spinors fail to describe excited states due to their inability to capture the corresponding electronic distribution. It has been recently demonstrated that a state-specific approach can mitigate this problem[57]. In this work, we present the theory, implementation, and benchmarking of a low-cost relativistic ADC(3) method for ionized, electron-attached, and excited states using the CD-X2CAMF Hamiltonian and frozen natural spinor approximation.

2 Theory

2.1 Relativistic Algebraic Diagrammatic Construction Theory

The algebraic–diagrammatic construction (ADC) method offers a systematic scheme for the calculations of generalized excitation energies[15, 16, 18, 27, 58–62] within the framework of propagator theory. The type of spectroscopic information obtained depends on the propagator under consideration. For instance, employing ADC in connection with the polarization propagator provides access to electronic excitation spectra,[16, 18, 29, 30, 58, 63], whereas the formulation based on the electron propagator enables the calculation of ionization potentials and electron affinities.[17, 27, 31, 58, 64, 65]

In the original formulation, the method did not provide access to explicit excited-state wave functions; only excitation energies and transition strengths could be extracted, obtained from the poles and residues of the propagator, respectively. This limitation was later resolved

through the development of the intermediate-state representation (ISR) framework.[14, 15, 18, 58, 66] The construction of intermediate state representations typically begins with the correlated excited states (CES),

$$|\Psi_J^0\rangle = \hat{C}_J|\Psi_0\rangle, \quad (1)$$

obtained by applying excitation operators \hat{C}_J on the correlated ground state $|\Psi_0\rangle$. The operator form depends on the propagator and the associated property: for the polarization propagator (PP), they generate particle-hole excitations that yield excitation energies, while for the electron propagator, they describe ionization or electron attachment processes leading to ionization potentials (IP)/electron attachment(EA):

$$EE : \quad \hat{C}_J = \hat{a}_a^\dagger \hat{a}_i; \hat{a}_a^\dagger \hat{a}_i \hat{a}_b^\dagger \hat{a}_j; a < b, i < j; \dots \quad (2)$$

$$IP : \quad \hat{C}_J = \hat{a}_i; \hat{a}_a^\dagger \hat{a}_i \hat{a}_j; i < j; \dots \quad (3)$$

$$EA : \quad \hat{C}_J = \hat{a}_a^\dagger; \hat{a}_a^\dagger \hat{a}_b^\dagger \hat{a}_j; a < b; \dots \quad (4)$$

The occupied orbitals are denoted by i, j, \dots , virtual orbitals by a, b, \dots , and p, q, \dots denote general indices. Excitations can be organized into μ -hole- μ -particle ($\mu h-\mu p$) classes, with μ counting the number of creation and annihilation operators; an analogous classification applies in the IP and EA case. Each excitation J is assigned a class $[J]$, with the ground state belonging to the zeroth class, $[J] = 0$.

The correlated excited states in Eq. (1) are generally nonorthogonal.[14] A two-step orthogonalization procedure is used to orthogonalize them.[15]. In the first step, a Gram-Schmidt (GS) orthogonalization is employed on the correlated excited state to generate precursor states.

$$|\Psi_J^\#\rangle = |\Psi_J^0\rangle - \sum_{K [K] < [J]} |\tilde{\Psi}_K\rangle \langle \tilde{\Psi}_K | \Psi_J^0\rangle, \quad (5)$$

and the resulting precursor states are made mutually orthonormal by symmetric orthogo-

nalization,

$$|\tilde{\Psi}_I\rangle = \sum_{J[J]=I} |\Psi_J^\#\rangle S_{IJ}^{-1/2}, \quad (6)$$

where $S_{IJ} = \langle \Psi_I^\# | \Psi_J^\# \rangle$ is the overlap matrix. The resulting intermediate states form a complete orthonormal basis for constructing the ISR secular matrix \mathbf{M} .

$$M_{IJ} = \langle \tilde{\Psi}_I | \hat{H}^{4c} - E_0 | \tilde{\Psi}_J \rangle, \quad (7)$$

which represents the shifted Hamiltonian $\hat{H}^{4c} - E_0$ in this intermediate-state basis and \hat{H}_{4c} is the four-component Dirac Coulomb Hamiltonian.

$$\hat{H}^{4c} = \sum_{pq} h_{pq}^{4c} \hat{a}_p^\dagger \hat{a}_q + \sum_{pqrs} \frac{1}{4} g_{pqrs}^{4c} \hat{a}_p^\dagger \hat{a}_q^\dagger \hat{a}_s \hat{a}_r \quad (8)$$

The exact eigenstates $|\Psi_n^N\rangle$ can then be expressed as linear combinations of the intermediate states,

$$|\Psi_n^N\rangle = \sum_J X_{In} |\tilde{\Psi}_I\rangle, \quad (9)$$

where the coefficients X_{In} are obtained from the eigenvectors of \mathbf{M} . In compact matrix notation, the secular equation of the ISR takes the form

$$\mathbf{M}\mathbf{X} = \mathbf{X}\mathbf{\Omega}, \quad \mathbf{X}^\dagger \mathbf{X} = \mathbf{1}, \quad (10)$$

with $\mathbf{\Omega}$ containing the excitation energies on the diagonal. The secular matrix in Eq. (10) can be expanded in a perturbative series. By truncating expansion at a chosen perturbation order (n), one obtains the ADC(n) working equations:

$$\mathbf{M} = \mathbf{M}^{(0)} + \mathbf{M}^{(1)} + \mathbf{M}^{(2)} + \mathbf{M}^{(3)} + \dots \quad (11)$$

For instance, restricting the series to second order gives the ADC(2) approximation, whereas

including terms up to the third order results in ADC(3). Dreuw and co-workers [67] introduced a mixed order variant, known as the scaled matrix ADC(sm-ADC) approach, in which the third-order matrix contribution is scaled by an ad hoc coefficient (x):

$$\mathbf{M}_{\text{sm-ADC}[(2)+x(3)]} = \mathbf{M}^{(0)} + \mathbf{M}^{(1)} + \mathbf{M}^{(2)} + x, \mathbf{M}^{(3)} \quad (12)$$

The scaling constant (x) can be varied between 0 and 1. Choosing ($x = 0$) recovers ADC(2), while ($x = 1$) corresponds to ADC(3). Based on our previous studies[38, 68], a choice of ($x = 0.5$) is used for the present study.

2.2 Properties in ISR formulation

The ISR framework described above can be naturally extended to operators other than the Hamiltonian. Let us consider a generic one-particle Hermitian operator \hat{D} , which corresponds to a physical observable of interest. In the language of second quantization, such an operator can be written as

$$\hat{D} = \sum_{pq} d_{pq} \{c_p^\dagger c_q\}, \quad (13)$$

Here, d_{pq} represent the matrix elements of the operator \hat{D} expressed in the Dirac–Hartree–Fock (DHF) spinor basis $\{\chi_p\}$,

$$d_{pq} = \langle \chi_p | \hat{D} | \chi_q \rangle, \quad (14)$$

and the notation with curly braces signifies normal ordering with respect to the reference determinant.

To determine a first-order property of a specific excited state corresponding to the operator \hat{D} , one needs to evaluate its expectation value, which is given by

$$D_K = \langle \Psi_K^{\text{ex}} | \hat{D} | \Psi_K^{\text{ex}} \rangle. \quad (15)$$

In practice, the contributions from the ground and excited states are treated separately. Within the ISR framework, the expectation value of the operator shifted by the ground-state contribution, $(\hat{D} - D_0)$, can be written as

$$\bar{D}_K = \sum_{IJ} Y_{IK}^* \langle \tilde{\Psi}_I | \hat{D} - D_0 | \tilde{\Psi}_J \rangle Y_{JK} = Y_K^* G Y_K \quad (16)$$

where the elements of the matrix \mathbf{G} are defined by

$$G_{IJ} = \langle \tilde{\Psi}_I | \hat{D} - D_0 | \tilde{\Psi}_J \rangle. \quad (17)$$

These matrix elements are often referred to as the modified excited-state transition moments.

To obtain the complete expectation value of the K th excited state, the ground-state contribution,

$$D_0 = \langle \Psi_0 | \hat{D} | \Psi_0 \rangle, \quad (18)$$

must be added to the expectation value of the shifted operator $(\hat{D} - D_0)$ given in Eq. (16). Accordingly, the total expectation value of the K th excited state can be expressed as

$$\bar{D}_K = \sum_{IJ} Y_{IK}^* \langle \tilde{\Psi}_I | \hat{D} - D_0 | \tilde{\Psi}_J \rangle Y_{JK} + \sum_{IJ} Y_{IK}^* \delta_{IJ} D_0 Y_{JK} \quad (19)$$

$$= Y_K^* G Y_K + D_0. \quad (20)$$

Where D_0 represents the ground-state component of the total excited-state property

$$D_0 = \text{Tr}(\rho d) \quad (21)$$

Here, ρ denotes the ground-state one-particle reduced density matrix, while d represents the matrix elements of the corresponding one-particle operator. To evaluate the ground-state

expectation value at the ADC(2) level, the density matrix must be expanded to include contributions up to second order in perturbation theory, i.e., $\rho = \rho^{(0)} + \rho^{(2)}$.^[13]

In addition to first-order properties of excited states, a key quantity of interest is the spectral intensity, which requires evaluating the transition properties between two states. The transition property from the ground state to the K^{th} excited state is defined as

$$T_{0 \rightarrow K} = \langle \Psi_K | \hat{D} - D_0 | \Psi_0 \rangle \quad (22)$$

Similarly, in the ISR formalism, it can be expressed as,

$$T_{0 \rightarrow K} = \sum_I Y_{IK}^* F_I \quad (23)$$

where,

$$F_I = \langle \tilde{\Psi}_I | \hat{D} | \Psi_0 \rangle \quad (24)$$

The \mathbf{F} and \mathbf{G} can be expanded in terms of the second quantized operators as,

$$F_I = \sum_{pq} f_{pq}^I d_{pq}, \quad G_{IJ} = \sum_{pq} g_{pq}^{IJ} d_{pq} \quad (25)$$

where,

$$f_{pq}^I = \langle \tilde{\Psi}_I | c_p^\dagger c_q | \Psi_0 \rangle, \quad g_{pq}^{IJ} = \langle \tilde{\Psi}_I | c_p^\dagger c_q | \tilde{\Psi}_J \rangle \quad (26)$$

One can describe the one-particle excited state reduced density matrix (ρ_{pq}^K) as

$$\rho_{pq}^K = \langle \Psi_K^{\text{ex}} | c_p^\dagger c_q | \Psi_K^{\text{ex}} \rangle = \sum_{IJ} Y_{IK}^* \langle \tilde{\Psi}_I | c_p^\dagger c_q | \tilde{\Psi}_J \rangle Y_{JK} = Y_K^* g_{pq} Y_K \quad (27)$$

and ground-to-excited state transition density matrix ($\rho_{pq}^{0 \rightarrow K}$) as

$$\rho_{pq}^{0 \rightarrow K} = \langle \Psi_K^{\text{ex}} | c_p^\dagger c_q | \Psi_0 \rangle = \sum_I Y_{IK}^* \langle \tilde{\Psi}_I | c_p^\dagger c_q | \Psi_0 \rangle = Y_K^* f_{pq} \quad (28)$$

By contracting these one-particle reduced density matrices with the corresponding one-particle operator, the properties of the excited states and the transition properties can be computed as

$$D_n = \langle \Psi_K^{\text{ex}} | \hat{D} | \Psi_K^{\text{ex}} \rangle = \sum_{pq} d_{pq} \rho_{pq}^K \quad (29)$$

$$T_{0 \rightarrow K} = \langle \Psi_K^{\text{ex}} | \hat{D} | \Psi_0 \rangle = \sum_{pq} d_{pq} \rho_{pq}^{0 \rightarrow K} \quad (30)$$

2.3 The X2CAMF approximation

Under the spin-separation scheme[69], the two-electron part of the four-component Dirac–Coulomb Hamiltonian (\hat{H}^{4c}) can be split into spin-free (SF) and spin-dependent (SD) contributions:

$$\hat{H}^{4c} = \sum_{pq} h_{pq}^{4c} \hat{a}_p^\dagger \hat{a}_q + \frac{1}{4} \sum_{pqrs} g_{pqrs}^{4c, \text{SF}} \hat{a}_p^\dagger \hat{a}_q^\dagger \hat{a}_s \hat{a}_r + \frac{1}{4} \sum_{pqrs} g_{pqrs}^{4c, \text{SD}} \hat{a}_p^\dagger \hat{a}_q^\dagger \hat{a}_s \hat{a}_r \quad (31)$$

The spin-dependent part can be approximated through the atomic mean-field (AMF) scheme[70–73], which exploits the localized character of spin–orbit interactions:

$$\frac{1}{4} \sum_{pqrs} g_{pqrs}^{4c, \text{SD}} \hat{a}_p^\dagger \hat{a}_q^\dagger \hat{a}_s \hat{a}_r \approx \sum_{pq} g_{pq}^{4c, \text{AMF}} \hat{a}_p^\dagger \hat{a}_q = \sum_{pqiA} n_{iA} g_{p_i A q_i A}^{4c, \text{SD}} \hat{a}_p^\dagger \hat{a}_q \quad (32)$$

Here, A denotes individual atoms, i corresponds to occupied spinors on atom A , and n_{iA} are their occupations. Substituting Eq. (32) into Eq. (31) yields

$$\hat{H}^{4c} = \sum_{pq} h_{pq}^{4c} \hat{a}_p^\dagger \hat{a}_q + \frac{1}{4} \sum_{pqrs} g_{pqrs}^{4c, \text{SF}} \hat{a}_p^\dagger \hat{a}_q^\dagger \hat{a}_s \hat{a}_r + \sum_{pq} g_{pq}^{4c, \text{AMF}} \hat{a}_p^\dagger \hat{a}_q \quad (33)$$

The 4c Hamiltonian can then be transformed to a two-component picture via the relations between large- and small-component coefficients (X matrix) and between large-component

and two-component coefficients (R matrix):

$$C^S = XC^L \quad (34)$$

$$C^L = RC^{2c} \quad (35)$$

The spin-free two-electron contribution $g^{4c, \text{SF}}$ gets reduced to the non-relativistic Coulomb integrals g^{NR} , when the two-electron picture-change (2e-pc) corrections are neglected. The resulting two-component Hamiltonian in the X2CAMF approximation is

$$\hat{H}^{\text{X2CAMF}} = \sum_{pq} h_{pq}^{\text{X2C}} \hat{a}_p^\dagger \hat{a}_q + \frac{1}{4} \sum_{pqrs} g_{pqrs}^{\text{NR}} \hat{a}_p^\dagger \hat{a}_q^\dagger \hat{a}_s \hat{a}_r + \sum_{pq} g_{pq}^{2c, \text{AMF}} \hat{a}_p^\dagger \hat{a}_q \quad (36)$$

which may be compactly expressed in terms of an effective one-electron operator:

$$\hat{H}^{\text{X2CAMF}} = \sum_{pq} h_{pq}^{\text{X2CAMF}} \hat{a}_p^\dagger \hat{a}_q + \frac{1}{4} \sum_{pqrs} g_{pqrs}^{\text{NR}} \hat{a}_p^\dagger \hat{a}_q^\dagger \hat{a}_s \hat{a}_r \quad (37)$$

where $h^{\text{X2CAMF}} = h^{\text{X2C}} + g^{2c, \text{AMF}}$. The major benefit of this Hamiltonian is that it eliminates the need to construct relativistic two-electron integrals.

2.4 Cholesky decomposition

In the present work, the Cholesky decomposition (CD) approach is used for calculating two-electron integrals. Unlike density-fitting (DF) or resolution-of-identity (RI) methods[74, 75], CD does not rely on an auxiliary basis set. Under CD, the electron-repulsion integrals (ERIs) are factorized as

$$(\mu\nu|\kappa\lambda) \approx \sum_P^{n_{\text{CD}}} L_{\mu\nu}^P L_{\kappa\lambda}^P \quad (38)$$

where $\mu, \nu, \kappa, \lambda$ are atomic spinor indices, $L_{\mu\nu}^P$ are Cholesky vectors, and n_{CD} is their rank. In the one-step procedure adopted here, Cholesky vectors are generated iteratively by selecting the largest remaining diagonal elements of the ERI matrix, until this value falls below a

preset threshold (τ). The resulting vectors are then transformed into the molecular spinor basis:

$$L_{pq}^P = \sum_{\mu\nu} C_{\mu p}^* L_{\mu\nu}^P C_{\nu q} \quad (39)$$

From these molecular Cholesky vectors, antisymmetrized integrals are constructed as

$$\langle pq||rs\rangle = \sum_P^{n_{\text{CD}}} (L_{pr}^P L_{qs}^P - L_{ps}^P L_{qr}^P) \quad (40)$$

Although we are using the one-step procedure in the current work, but it is worth noting that an efficient two-step algorithm for the Cholesky decomposition of the electron-repulsion integrals has also been developed, in which only the elements of the Cholesky basis are generated during the pivoting procedure.[76–78]. In this implementation, four-external ($\langle ab||cd\rangle$) and three-external ($\langle ab||ci\rangle$) integrals are neither precomputed nor stored, but generated on the fly. All other integrals are explicitly constructed and stored in the truncated FNS basis. More details regarding the FNS and CD-based X2CAMF implementation of relativistic coupled-cluster methods are available in Ref. [56].

2.5 Frozen natural spinors

Natural spinors[56, 79–82] are the relativistic analogues of the natural orbitals introduced by Löwdin[83]. These are obtained as the eigenfunctions of the correlated one-particle reduced density matrix[84]. In ground-state energy computations, natural spinors are typically obtained from the first-order Møller–Plesset (MP1) wave function. Within the frozen natural spinor (FNS) scheme, only the virtual space is optimized using natural spinors, while the occupied space is retained at the Dirac–Hartree–Fock (DHF) level. After the SCF step, a partial AO–MO integral transformation is carried out to form integrals with two external indices. From this, the virtual–virtual block of the one-particle reduced density matrix at

the MP2 level can be obtained as

$$D_{ab} = \frac{1}{2} \sum_{cij} \frac{\langle ac||ij\rangle \langle ij||bc\rangle}{\varepsilon_{ij}^{ac} \varepsilon_{ij}^{bc}} \quad (41)$$

Diagonalization of this virtual–virtual density block (D_{ab}) yields the virtual natural spinors (VNS) as eigenvectors V and their corresponding occupation numbers as eigenvalues η :

$$D_{ab}V = V\eta \quad (42)$$

Virtual spinors with small occupation numbers can be discarded using a cutoff η_{crit}

$$\tilde{V} = VT \quad (43)$$

where $T_{ij} = \delta_{ij}$ if $\eta_i \geq \eta_{crit}$, and $T_{ij} = 0$ otherwise. The virtual–virtual block of the Fock matrix is then projected into this truncated natural spinor basis

$$\tilde{F} = \tilde{V}^\dagger F \tilde{V} \quad (44)$$

This transformed Fock matrix (\tilde{F}) is diagonalized to semi-canonicalize the truncated basis

$$\tilde{F}\tilde{Z} = \tilde{Z}\tilde{\epsilon} \quad (45)$$

The eigenvectors \tilde{Z} together with the retained natural spinors \tilde{V} form the overall transformation matrix (B) linking the canonical and truncated FNS bases

$$B = \tilde{V}\tilde{Z} \quad (46)$$

In the subsequent discussions, this procedure of constructing frozen natural spinors from MP2 densities will be referred to as the FNS scheme. While MP2-based natural spinors[56, 79–

81] are tailored to efficiently recover ground-state correlation energy, as well as ionization potential[54, 85], and double ionization potential calculations[86, 87], they are not well suited for excited states[57]. Even in the non-relativistic domain, there is no general consensus on defining optimal natural orbitals for excited states. Recently, we demonstrated that ADC(2) provides an accurate first-order description of the electron attached[68] and excited-state wave functions[57], and use of ADC(2)-based natural orbital gives consistent accuracy across valence, Rydberg, and charge-transfer excited states in the EOM-CCSD method[88].

The IP-ADC(3) calculations in this manuscript are done using standard MP2 FNS, and the EA and EE-ADC(3) calculations are done using the state-specific FNS(SS-FNS). The state-specific one-particle density matrices are calculated at the relativistic ADC(2) level[38, 89, 90]. For the k^{th} electron attached/ excited state, the virtual–virtual block of the density takes the form

$$D_{ab}^{SS}(k) = D_{ab}^{MP2} + D_{ab}^{EA/EE-ADC(2)}(k) \quad (47)$$

where D_{ab}^{MP2} represents the MP2-level virtual–virtual density block and $D_{ab}^{EA/EE-ADC(2)}(k)$ is the electron-attached/excited-state contribution from EA/EE-ADC(2). The zeroth-order intermediate state representation[13] with ADC(2) eigen vectors were used to obtain excited-state densities. The programmable expression for the state-specific density are provided in the supporting information. Inserting Eq. (47) into Eq. (42) and following Eqs. (42–46) produces the state-specific frozen natural spinor basis (SS-FNS) for each excited state, in which the ADC(3) calculations are subsequently performed. A schematic representation of the algorithm used for EA-ADC(3) and EE-ADC(3) has been presented in Figure1 in the supporting information.

A perturbative energy correction can be included by comparing EA/EE-ADC(2) energies in the canonical basis and the truncated SS-FNS basis. This correction is added to the uncorrected SS-FNS-EOM-CCSD electron affinity/excitation energy as

$$\omega_{SS-FNS-ADC(3)}^{corrected}(k) = \omega_{SS-FNS-ADC(3)}^{uncorrected}(k) + \omega_{ADC(2)}^{canonical}(k) - \omega_{ADC(2)}^{SS-FNS}(k) \quad (48)$$

To ensure that each root is solved in its corresponding SS-FNS basis, a root-specific Davidson solver[91] is employed. In this approach, overlaps of trial vectors with initial guesses are monitored to ensure correct root homing. The canonical ADC(2) eigenvectors are transformed to the corresponding SS-FNS basis, act as starting guesses for the subsequent ADC(2) and ADC(3) calculations in the SS-FNS basis. The perturbative correction has not been considered for the FNS-IP-ADC(3) method, as it has been shown that the perturbative correction does not lead to any appreciable improvement[92, 93]. In relativistic ADC(2)[38, 89, 90] calculations targeting electron attached/ excited states, one must additionally handle integrals with one, two, and three external indices in the canonical basis (beyond the two-external integrals needed in standard FNS). In the four-component Dirac–Coulomb (4c-DC) framework, three external integrals become a major bottleneck for large basis sets. Moreover, the full transformation of integrals—even in the truncated basis—must be repeated for every excited state, making this approach impractical for a direct four-component implementation. Therefore, to achieve computational feasibility, one needs to adopt additional approximations such as two-component Hamiltonians.

The FNS-IP-ADC(3) and SS-FNS-EA/EE-ADC(3) methods, based on the X2CAMF Hamiltonian, have been implemented in our in-house software package, BAGH. [94]. The BAGH is written in Python, with Cython and Fortran being used to optimize the computationally demanding parts. It is interfaced with PySCF[95–97], socutils[98], DIRAC[99] and GAMESS-US[100]. All the calculations presented here have been calculated using PySCF and socutils interface of BAGH.

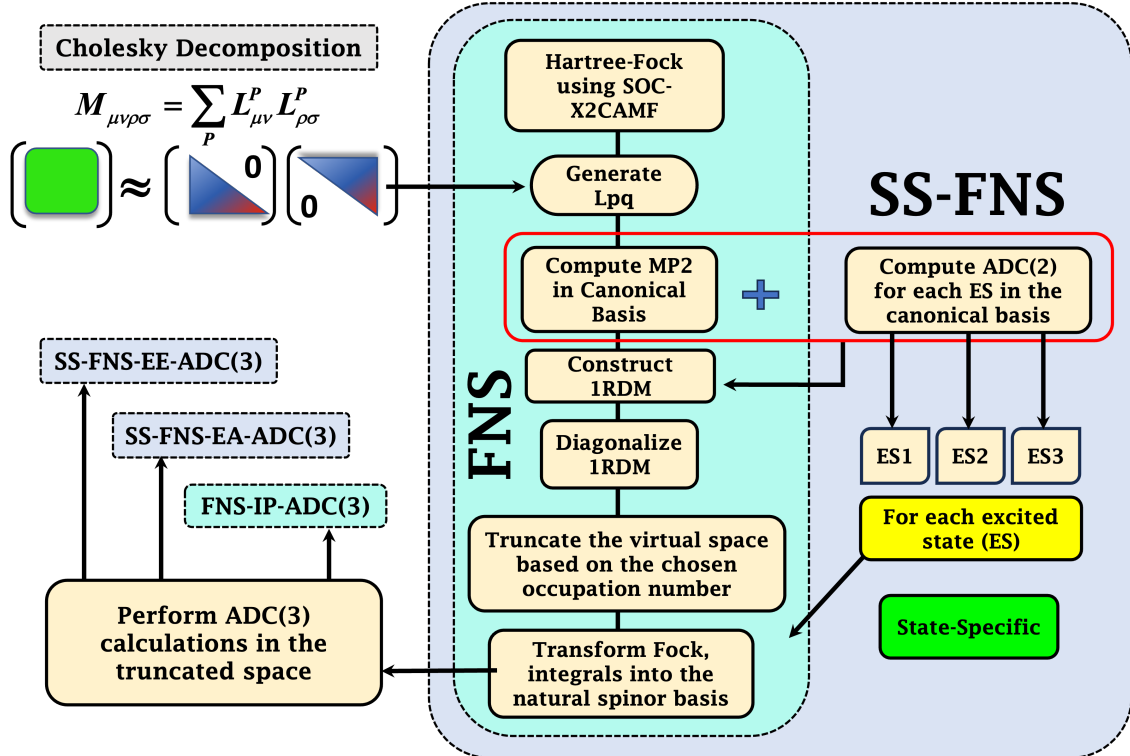


Figure 1: The schematic flowchart of CD based FNS-IP-ADC(3), SS-FNS-EE-ADC(3) and SS-FNS-EA-ADC(3).

3 Results and discussion

3.1 Ionization potential

3.1.1 Choice of truncation threshold

The accuracy of the FNS-based method depends upon the occupation threshold used for truncation. To get an appropriate FNS threshold, we have studied the convergence of IP values with respect to the FNS threshold for the first IP value of IBr (See Figure 2). The uncontracted dyall.v2z basis set has been used for the calculations. The CD threshold has been kept at 10^{-3} following reference [101]. It can be seen that the result almost converges at the threshold of $10^{-4.5}$. The error is even smaller at the threshold of 10^{-4} . Therefore, we have used the CD threshold 10^{-3} and FNS threshold of 10^{-4} for the subsequent calculation, which is similar to the LOOSEFNS threshold in reference [101].

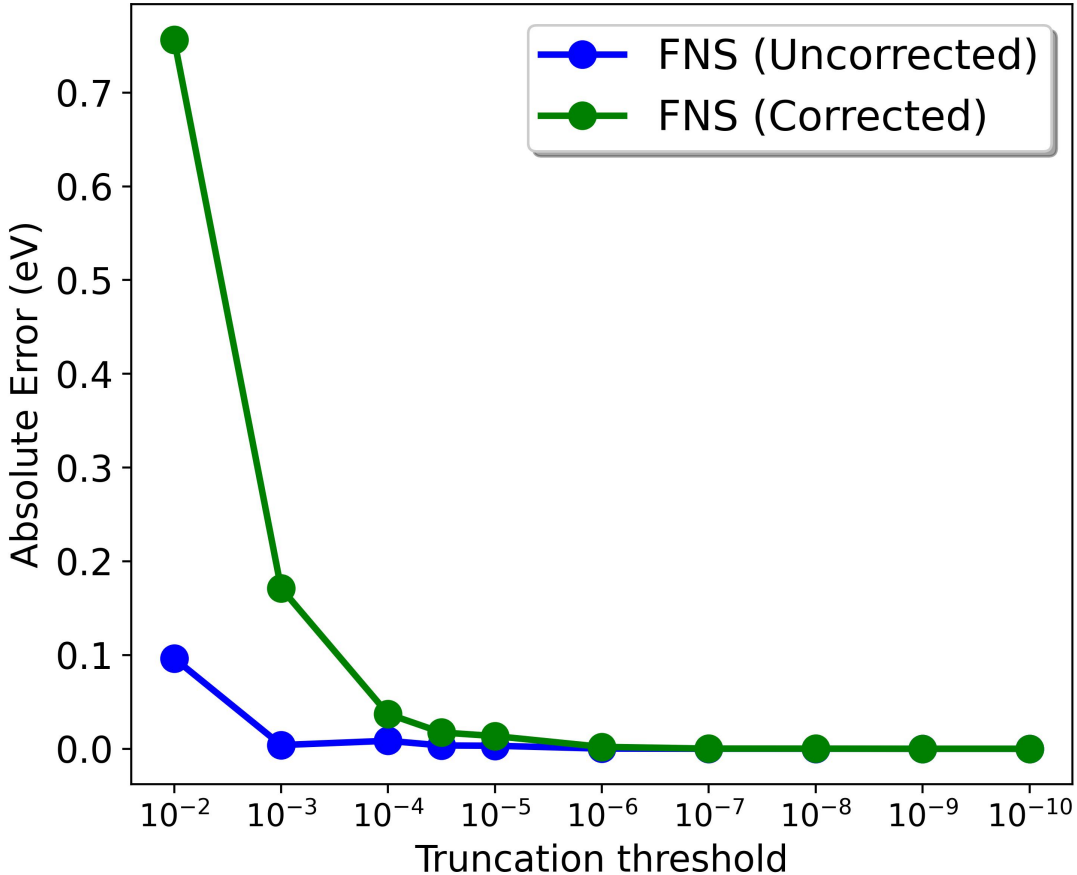


Figure 2: The comparison of absolute error in IP (in eV) for FNS truncation scheme of CD-based X2CAMF version of IP-ADC(3) with respect to the canonical result for IBr molecule using dyall.v2z basis set.

3.1.2 Performance on a standard test set

To further investigate the accuracy of the FNS-IP-ADC(3) method, we have calculated the vertical IP values of the molecules contained in the SOC-81 dataset. The FNS-CD-IP-ADC(3) calculations were performed using dyall.v4z basis set and the mean absolute error (MAE), mean error (ME), and standard deviation of errors (SE) relative to the corresponding experimental ionization potentials were analyzed. Recently, Zgid and co-workers [102] developed a relativistic variant of the fully self-consistent GW (scGW) method, incorporating spin-orbit coupling through the exact two-component (X2C) Coulomb approximation. They have applied both scGW and G_0W_0 approximation for the SOC-81 dataset, which

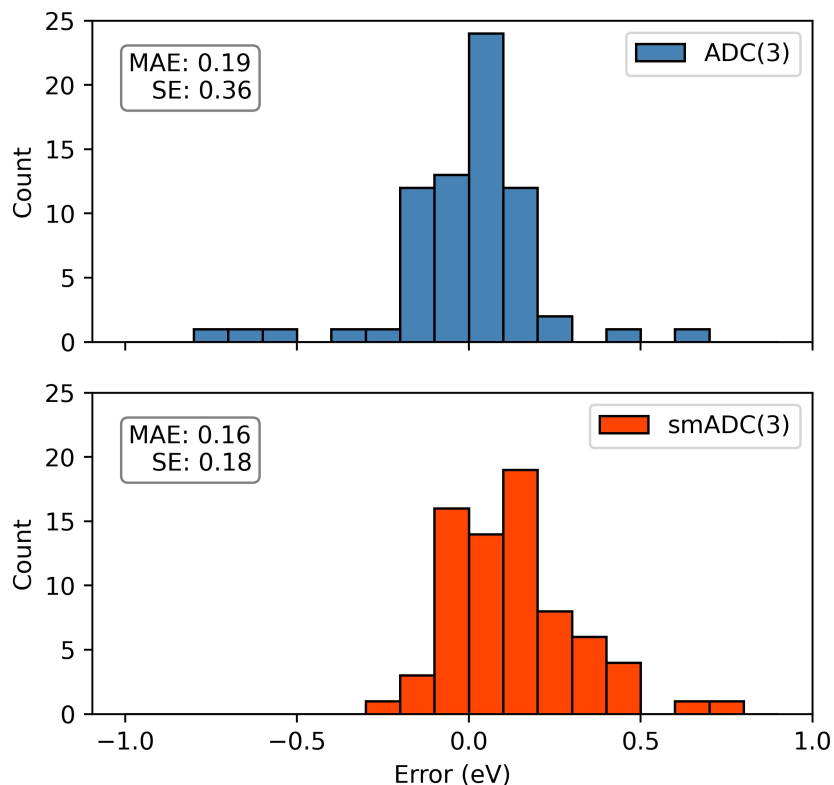


Figure 3: Histogram of errors with respect to experimental value for IP of molecules in SOC-81 dataset with standard FNS-CD-IP-ADC(3) (top) and semiempirically scaled FNS-CD-IP-smADC[(2)+x(3)] (bottom) where $x = 0.5$.

comprises closed-shell molecules containing heavy elements, and benchmarked their results against experimental first ionization potentials. To facilitate consistent comparison with the GW-based study by Zgid and co-workers, we adopted the same set of 74 molecules from the original SOC-81 dataset used in their benchmarking. In line with their protocol, we excluded seven molecules from the full set - MgI_2 , AsF_5 , AlBr_6 , $(\text{C}_5\text{H}_5)_2\text{Ru}$, $\text{Mo}(\text{CO})_6$, TiI_4 , and ZrI_4 from the statistical analysis to ensure a one-to-one correspondence in the comparison. We also incorporated the same corrections for experimental IP applied to HgCl_2 , KBr , and RbBr , where the originally reported IPs in the NIST database corresponded to the second IPs (due to spin-orbit splitting) rather than the first. The IP values of all the molecules, including the excluded molecules, were presented in Table S1 of the Supporting Information.

Table 1: Comparison of MAE, SE and ME of vertical IP of SOC-81 set using FNS-CD-IP-ADC(3) and previously reported methods with respect to experimental value. All values are in eV

Method	MAE	SE	ME
$G_0W_0@$ PBE	0.32	0.23	-0.31
$G_0W_0@$ PBE0	0.14	0.20	0.00
<i>scGW</i>	0.21	0.17	-0.17
FNS-CD-IP-ADC(3)	0.19	0.36	-0.07
FNS-CD-IP-[ADC(2)+x(3)]	0.16	0.18	0.12
FNS-CD-X2CAMF-IP-EOM-CCSD[101]	0.13	0.18	-0.02

In Table 1, we observe that the standard FNS-CD-IP-ADC(3) approach yields a mean absolute error (MAE) of 0.19 eV, with a mean error (ME) of -0.07 eV, indicating an underestimation compared to the experimental IPs. However, the standard error (SE) is 0.36 eV, suggesting a somewhat larger variance in error across the dataset. The results are inferior compared to the corresponding EOM-CCSD values. However, the scaled matrix FNS-CD-IP-[ADC(2)+x(3)] method, where the third-order ADC contribution is scaled with an empirical factor, $x = 0.5$ gives an excellent performance and achieves an improved MAE of 0.16 eV and a lower SE of 0.18 eV. The histogram analysis in Figure 3 further supports this trend, showing tighter clustering of errors around the experimental benchmark in FNS-CD-IP-[ADC(2)+x(3)] method. To contextualize our findings, we benchmarked both ADC-based methods against GW-based approaches applied to the same SOC-81 subset. Table 1 compiles the MAE, SE, and ME obtained from one-shot and self-consistent GW approaches, $G_0W_0@$ PBE, $G_0W_0@$ PBE0, and *scGW*, each implemented with exact two-component (X2C) relativistic Hamiltonian. The $G_0W_0@$ PBE scheme performs worst (MAE = 0.32 eV, ME = -0.31 eV), whereas $G_0W_0@$ PBE0 improves accuracy (MAE = 0.14 eV, ME = 0.00 eV, SE = 0.20 eV), highlighting sensitivity of G_0W_0 method on the selection of DFT functional. Fully self-consistent *scGW* yields an intermediate MAE of 0.21 eV (ME = -0.17 eV, SE = 0.17 eV) but at substantially higher cost due to iterative Dyson-equation solutions. The FNS-CD-IP-[ADC(2)+x(3)] method exhibit comparable or superior accuracy compared to

GW techniques while retaining significant computational advantages. The low MAE and SE values underscore the efficacy of combining frozen natural spinors with semi-empirical scaling for reliable IP predictions in molecular systems where relativistic effects are relevant.

3.1.3 Comparison with four-component results

Table 2: Spin-orbit splitting (eV) of halogen oxides calculated with different methods.

Molecule	Method	${}^2\Pi_{3/2}$	$N_{v,act}$	${}^2\Pi_{1/2}$	Splitting	Expt	Error ^c
ClO ⁻	4c-IP-ADC(3) ^a	2.4158		2.4659	0.0502	0.0397	0.0105
	4c-IP-ADC[(2)+x(3)] ^a	1.7446		1.7862	0.0416		0.0019
	4c-IP-EOM-CCSD ^a				0.0422		0.0025
	FNS-CD-IP-ADC(3) ^a	2.3367	106	2.3862	0.0495		0.0098
	FNS-CD-IP-ADC[(2)+x(3)] ^a	1.7087	106	1.7499	0.0412		0.0015
	FNS-CD-IP-ADC(3) ^b	2.3949	112	2.4476	0.0527		0.0130
	FNS-CD-IP-ADC[(2)+x(3)] ^b	1.7687	112	1.8090	0.0403		0.0006
BrO ⁻	4c-IP-ADC(3) ^a	2.5819		2.7470	0.1651	0.1270	0.0381
	4c-IP-ADC[(2)+x(3)] ^a	1.9125		2.0347	0.1222		0.0048
	4c-IP-EOM-CCSD ^a				0.1294		0.0024
	FNS-CD-IP-ADC(3) ^a	2.5305	132	2.6925	0.1620		0.0350
	FNS-CD-IP-ADC[(2)+x(3)] ^a	1.8923	132	2.0130	0.1207		0.0063
	FNS-CD-IP-ADC(3) ^b	2.5347	154	2.7004	0.1657		0.0387
	FNS-CD-IP-ADC[(2)+x(3)] ^b	1.9337	154	2.0530	0.1193		0.0077
IO ⁻	4c-IP-ADC(3) ^a	2.5889		2.9760	0.3871	0.2593	0.1278
	4c-IP-ADC[(2)+x(3)] ^a	2.0161		2.2791	0.2630		0.0037
	4c-IP-EOM-CCSD ^a				0.2776		0.0183
	FNS-CD-IP-ADC(3) ^a	2.5880	140	2.9674	0.3794		0.1201
	FNS-CD-IP-ADC[(2)+x(3)] ^a	2.0231	140	2.2792	0.2561		0.0032
	FNS-CD-IP-ADC(3) ^b	2.5184	172	2.9171	0.3987		0.1394
	FNS-CD-IP-ADC[(2)+x(3)] ^b	2.0683	172	2.3235	0.2552		0.0041

^a X: dyall.acv3z, O: uncontracted aug-cc-pVTZ.

^b X: dyall.acv4z, O: uncontracted aug-cc-pVQZ.

^c Error with respect to the experiment.

Table 2 presents the spin-orbit splittings of the halogen oxide anions XO⁻ (X=Cl, Br, I) obtained with various relativistic electron detachment methods, and compares them against available experimental and previously reported theoretical values. The focus here is on

the performance of the FNS-CD variants of IP-ADC in relation to the conventional four-component (4c) implementations. The spin-orbit splittings of halogen monoxide anions (XO^- ; $\text{X} = \text{Cl}, \text{Br}, \text{and I}$) were calculated using the Dyall.acv3z basis set for the halogen atom (X) and an uncontracted aug-cc-pVTZ basis set for the oxygen atom. The results in Table 2 show that the FNS-CD-IP-ADC(3) methods based on X2CAMF Hamiltonian reproduce the 4c values with very good accuracy while substantially reducing the computational cost through a truncated virtual space. Across ClO^- , BrO^- , and IO^- , the FNS-CD-IP-ADC(3) splittings are consistently within 0.003–0.005 eV of their 4c-IP-ADC(3) counterparts, regardless of the basis set. A similar trend is observed for the semiempirical FNS-CD-IP-ADC[(2)+x(3)], which follows the 4c results almost one-to-one, typically differing by less than 0.002 eV in the splitting values. Compared to experiment, both 4c and FNS-CD variants at the standard ADC(3) level tend to deviate more, especially for the heavier IO^- , while the scaled matrix [(2)+x(3)] treatment significantly improves agreement and yields errors on the order of a few meV. Thus, FNS-CD offers a reliable and computationally more affordable alternative to 4c calculations without sacrificing accuracy in describing spin-orbit splittings.

3.2 Excitation energy

Determining an appropriate truncation threshold is essential prior to performing reliable excitation energy calculations. To this end, we selected Gold Hydride (AuH) as a benchmark system to investigate the dependence of excitation energies on the truncation threshold. Specifically, we focused on the $0^+(\text{II})$ excited state, for which experimental excitation energy data are available. Figure 4 illustrates the variation of absolute error in excitation energy (in eV) as a function of the truncation threshold, comparing three computational schemes: SS-FNS-EE-ADC(3), perturbatively corrected SS-FNS-EE-ADC(3), and FNS-EE-ADC(3), denoted as SS-FNS (Uncorrected), SS-FNS (Corrected), and FNS, respectively. The singly augmented dyall.v2z basis set is used for Au, and the uncontracted aug-cc-pVDZ basis set

is used for H in the calculations. It is evident that the FNS method exhibits a significant dependence on the truncation threshold. At 10^{-2} thresholds (10^{-2}), the absolute error is large, nearly 8 eV. However, the error decreases rapidly with tighter thresholds, reaching below 0.1 eV at the threshold of 10^{-6} , and eventually plateauing with negligible error as the threshold tightens further. In contrast, both SS-FNS (Uncorrected) and SS-FNS (Corrected) show consistently low errors across the entire range of truncation thresholds.

3.2.1 Choice of truncation threshold

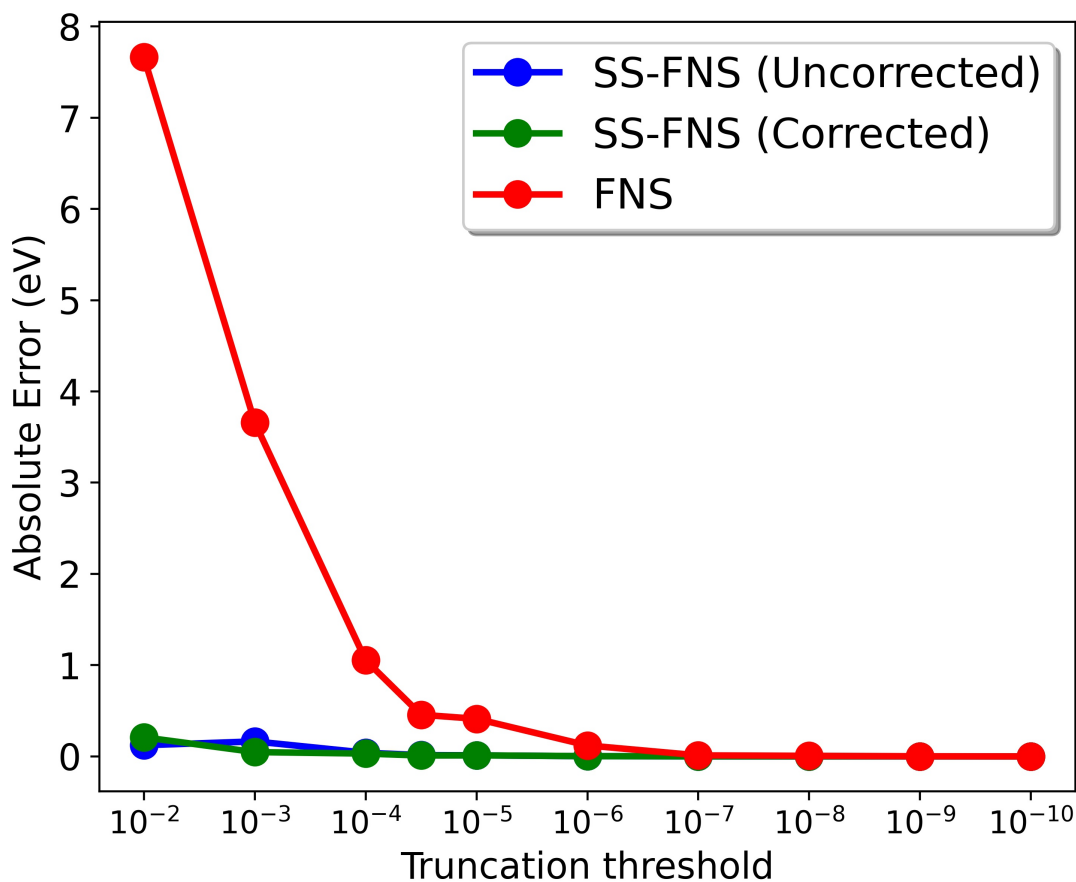


Figure 4: The comparison of absolute error in excitation energies (in eV) for FNS and SS-FNS truncation schemes of CD-based X2CAMF version of EE-ADC(3) with respect to the canonical result for AuH molecule ($0^+(\text{II})$ state) in singly augmented dyall.v2z basis set for Au and uncontracted aug-cc-pVDZ basis set for H at different truncation thresholds.

The SS-FNS method maintains a relatively stable error profile, with errors staying below 0.2 eV even at 10^{-2} , and gradually reducing to less than 0.01 eV at tighter thresholds. The inclusion of perturbative corrections improves the convergence behavior of the SS-FNS-ADC(3) method, although its effect is small. It confirms that the SS-FNS-EE-ADC(3) scheme is not only accurate but also stable with respect to the choice of truncation threshold. In contrast, the FNS approach requires a very tight threshold (e.g., 10^{-6} or better) to achieve comparable accuracy, making it less practical in such contexts. It is noteworthy that at a truncation threshold of $10^{-4.5}$ the SS-FNS-EE-ADC(3) approach retains 132 out of 382 virtual spinors, corresponding to a truncation of approximately 65% of the virtual space. Under the same threshold, the FNS-ADC(3) method retains 128 virtual spinors, a 66% truncation. Despite the comparable levels of truncation, the corrected SS-FNS-EE-ADC(3) scheme achieves markedly superior accuracy, exhibiting an absolute error of only 0.0096 eV, in contrast to the significantly larger error of 0.46 eV observed for the FNS-ADC(3) approach. This highlights the efficacy of the relativistic SS-FNS-EE-ADC(3) in reliably recovering canonical-level accuracy even under aggressive truncation conditions. A truncation threshold of $10^{-4.5}$ has been employed for all subsequent excitation energy calculations across atoms and molecules in this section.

3.2.2 Excitation energies and fine-structure splitting of Ga⁺, In⁺, and Tl⁺

Table 3 presents a comparative analysis of the excitation energies (in eV) of group 13 cations Ga⁺, In⁺, and Tl⁺ obtained using the SS-FNS-EE-ADC(3) method, the fully relativistic four-component EE-ADC(3), and experimental values. Calculations were performed using the triply augmented dyall valence triple-zeta (t-aug-dyall.v3z) basis set. Virtual spinors with energies up to 2000 Eh were included in the correlation treatment, and the frozen-core approximation was applied to all atoms. This resulted in 278, 300, and 402 virtual spinors for the canonical calculations Ga⁺, In⁺, and Tl⁺, respectively. For all three ions, the four low-lying excited states—namely 3P_0 , 3P_1 , 3P_2 , and 1P_1 —were investigated. For

Table 3: Comparison of excitation energies (in eV) of Ga⁺, In⁺, and Tl⁺ from SS-FNS-EE-ADC(3), 4c-EE-ADC(3), and experiment using t-aug-dyall.v3z.

		SS-FNS-EE-ADC(3)		SS-FNS-EE-ADC[(2)+x(3)]		4c-EE-ADC(3)	Expt.
		Uncorrected	Corrected	Uncorrected	Corrected	Canonical	
Ga ⁺	$^1S_0 \rightarrow ^3P_0$	5.545	5.550	5.469	5.474	5.534	5.874
	$^1S_0 \rightarrow ^3P_1$	5.599	5.604	5.523	5.528	5.589	5.928
	$^1S_0 \rightarrow ^3P_2$	5.713	5.718	5.632	5.639	5.702	6.044
	$^1S_0 \rightarrow ^1P_1$	8.628	8.618	8.669	8.659	8.610	8.766
	Splitting						
	$^3P_0 \rightarrow ^3P_1$	0.054	0.054	0.054	0.054	0.054	0.055
	$^3P_1 \rightarrow ^3P_2$	0.114	0.114	0.109	0.111	0.113	0.116
In ⁺	$^1S_0 \rightarrow ^3P_0$	4.855	4.858	4.796	4.799	4.851	5.242
	$^1S_0 \rightarrow ^3P_1$	4.986	4.989	4.926	4.930	4.982	5.375
	$^1S_0 \rightarrow ^3P_2$	5.280	5.283	5.218	5.221	5.275	5.682
	$^1S_0 \rightarrow ^1P_1$	7.686	7.673	7.726	7.714	7.673	7.816
	Splitting						
	$^3P_0 \rightarrow ^3P_1$	0.131	0.131	0.130	0.131	0.131	0.133
	$^3P_1 \rightarrow ^3P_2$	0.294	0.294	0.292	0.291	0.293	0.307
Tl ⁺	$^1S_0 \rightarrow ^3P_0$	5.982	5.981	6.137	6.137	5.983	6.131
	$^1S_0 \rightarrow ^3P_1$	6.345	6.342	6.498	6.496	6.344	6.496
	$^1S_0 \rightarrow ^3P_2$	7.449	7.450	7.584	7.586	7.451	7.653
	$^1S_0 \rightarrow ^1P_1$	9.219	9.213	9.407	9.401	9.221	9.381
	Splitting						
	$^3P_0 \rightarrow ^3P_1$	0.363	0.362	0.361	0.359	0.361	0.365
	$^3P_1 \rightarrow ^3P_2$	1.104	1.107	1.086	1.090	1.107	1.157

all three atoms, both the uncorrected and corrected SS-FNS-EE-ADC(3) excitation energies are in close agreement with each other, differing only in the third decimal place. Comparison with the fully relativistic 4c-EE-ADC(3) results reveals that the SS-FNS-EE-ADC(3) approach—especially the corrected variant—offers a consistent approximation to the fully relativistic treatment, with deviations typically within $\tilde{0}.01$ – 0.02 eV. All the versions of ADC(3) methods, however, underestimate the excitation energies compared to experiment, which may be attributed to the absence of higher-order correlation and QED effects. For example, in Ga⁺, the $^1S_0 \rightarrow ^3P_0$ transition energy is underestimated by approximately 0.32 eV by the 4c-EE-ADC(3) method. The use of ADC[(2)+x(3)] approximation does not show any appreciable improvement over the standard ADC(3) method. The calculated fine structure splittings between the 3P_J states show excellent agreement with the experimental data. For

all three cations, both SS-FNS-EE-ADC(3) and 4c-EE-ADC(3) reproduce the small energy gaps between ${}^3P_0 \rightarrow {}^3P_1$ and ${}^3P_1 \rightarrow {}^3P_2$ transitions with deviations well below 0.01 eV. The largest splitting, seen in Tl^+ (1.104–1.107 eV), is also accurately captured, demonstrating the ability of both approaches to account for spin-orbit coupling effects in heavy elements. The use of larger t-aug-dyall.v4z basis set leads to improvement in the excitation energy values, but the improvement in fine structure splitting is negligible (See Table S2).

3.2.3 Excitation energy of I_3^- molecule

Table 4: Comparison of excitation energies (in eV) of I_3^- ion calculated using X2CAMF-SS-EE-ADC(3) and smADC-EE-ADC(3) methods with the dyall.av3z basis set, compared to relativistic 4c-DC-EE-ADC(3) canonical results.

State	Ω	4c-DC-EOM-CCSD[103]	4c-DC-EE-ADC(3)	SS-FNS-EE-ADC(3)		SS-FNS-EE-ADC[(2)+x(3)]		SS-FNS-EE-EOM-CCSD		N_{vir}
		canonical	canonical	Uncorrected	Corrected	Uncorrected	Corrected	Uncorrected	Corrected	
1	2_g	2.24	2.06	2.07	2.07	2.21	2.21	2.27	2.26	254
2	1_g	2.37	2.19	2.20	2.19	2.41	2.40	2.41	2.40	256
3	0_u^-	2.37	2.23	2.23	2.23	2.41	2.41	2.41	2.41	254
4	1_u	2.38	2.23	2.24	2.24	2.34	2.34	2.40	2.40	254
5	0_g^-	2.84	2.66	2.67	2.67	2.81	2.81	2.86	2.86	254
6	0_g^+	2.89	2.71	2.71	2.71	2.87	2.86	2.92	2.91	254
7	1_g	3.07	2.87	2.88	2.88	3.03	3.03	3.09	3.08	256
8	2_u	3.32	3.13	3.13	3.13	3.27	3.27	3.35	3.34	256
9	1_u	3.41	3.19	3.20	3.19	3.35	3.35	3.43	3.42	256
10	0_u^+	3.66	3.43	3.44	3.44	3.60	3.59	3.68	3.67	262
11	2_g	4.09	3.88	3.89	3.89	4.06	4.06	4.12	4.12	258
12	0_u^-	4.08	3.89	3.90	3.90	4.19	4.18	4.10	4.09	254
13	1_u	4.18	3.96	3.97	3.97	4.04	4.04	4.20	4.19	260
14	1_g	4.21	3.99	3.99	3.99	4.14	4.13	4.24	4.23	256
15	0_u^+	4.49	4.28	4.29	4.29	4.67	4.67	4.50	4.49	266
16	0_g^-	4.69	4.49	4.50	4.50	4.43	4.43	4.72	4.71	256
17	0_g^+	4.70	4.50	4.51	4.50	4.68	4.68	4.73	4.72	256
18	1_g	4.90	4.85	4.95	4.93	4.99	4.97	4.94	4.93	266
MAD				0.013	0.010					
STD				0.022	0.018					
RMSD				0.025	0.020					

Table 4 presents a comparison of excitation energies (in eV) for the I_3^- ion, computed using the X2CAMF-SS-FNS-EE-ADC(3) method with the dyall.av3z basis set. These values are benchmarked against 4c-EE-ADC(3) results, which serve as a reference. Following our previous work on relativistic ADC(3), all calculations in this study were performed using the dyall.av3z basis set. Following reference[103], a total of 52 electrons were correlated, and all spinors with orbital energies in the range of -3.0 to 12.0 E_h were included, resulting in 332 virtual spinors in the canonical space. For each excited state, both uncorrected and per-

turbatively corrected excitation energies obtained from the SS-FNS formalism are reported, along with the number of active virtual spinors (N_{vir}) retained in the truncated virtual space. The uncorrected SS-FNS-EE-ADC(3) results show excellent agreement with the 4c-ADC(3) excitation energies across all 18 excited states considered. The maximum deviation is minimal, and the state ordering remains consistent throughout. The inclusion of the perturbative correction further improves the results, leading to a slight reduction in the overall deviation from the 4c reference values. In many cases, the corrected excitation energies are numerically indistinguishable from the uncorrected ones, indicating that the dominant contributions are already captured accurately within the SS-FNS space. To quantitatively assess accuracy, we computed the mean absolute deviation (MAD), standard deviation (STD), and root mean square deviation (RMSD) relative to the 4c results. The uncorrected SS-FNS-ADC(3) yields a MAD of 0.0128 eV, STD of 0.0216 eV, and RMSD of 0.0251 eV. Upon applying the perturbative correction, these values slightly improve to a MAD of 0.0100 eV, STD of 0.0176 eV, and RMSD of 0.0203 eV. These small deviations indicate the accuracy and reliability of the SS-FNS-ADC(3) framework in describing relativistic excitation spectra. In addition to the numerical accuracy, the SS-FNS approach offers significant computational savings by operating in a reduced virtual space (e.g., 254–266 virtual spinors versus 332 in the full canonical basis). The standard SS-FNS-ADC(3) results show significant deviation as compared to the EOM-CCSD values, whereas the SS-FNS-EE-ADC[(2)+x(3)] method shows good agreement with the latter.

3.2.4 Transition properties of Xe atom

Table 5 reports the excitation energies (EE) and transition dipole moments (TDMs) for selected excited states of the xenon atom, calculated using SS-FNS-EE-ADC(3) and 4c-EE-ADC(3), and compared against experimental data. The calculations employed the d-aug-Dyall.ae3z basis set, with the frozen-core approximation and a virtual spinor energy cutoff of 361 Eh. This setup yields a correlation space of 18 occupied and 364 virtual spinors.

The same basis set and the correlation space are used as in our previous 4c-EE-ADC(3) implementation.[38]. The SS-FNS-EE-ADC(3) closely reproduces both the EEs and TDMs obtained from 4c-EE-ADC(3). The deviations between SS-FNS and 4c are within 0.03 eV for EEs and less than 0.005 a.u. for TDMs, indicating that in the SS-FNS framework, the truncated virtual space is sufficient to capture the essential correlation and relativistic effects for these transitions. Interestingly, with a truncation threshold of $10^{-4.5}$, approximately 56% of the 364 virtual spinors are excluded, leaving only 158 active virtual spinors for the SS-FNS-EE-ADC(3) calculations. However, the performance of SS-FNS-EE-ADC(3) is mixed compared to the experimental results. The calculated transition moment shows good agreement with the experimental results except for the $5p^5(^2P_{3/2})5d,^2[3/2]_1^o$ states. However, the excitation energy values are significantly underestimated as compared to the experiments for all states. The performance is similar to that of the canonical 4c-ADC(3) method. The excitation energy values can be improved by using the scaled matrix SS-FNS-EE-ADC[(2)+x(3)] method. However, the agreement with experiment for transition moment significantly deteriorates on using SS-FNS-EE-ADC[(2)+x(3)]. The trend is consistent with that observed by Dreuw and co-workers [67] for the non-relativistic case.

Table 5: Comparison of transition dipole moments (TDM in a.u.) for selected excited states of the Xe atom obtained using different methods using d-aug-dyall.ae3z.

State	SS-FNS-EE-ADC(3)			SS-FNS-EE-ADC[(2)+x(3)]			4c-EE-ADC(3)		Expt.	
	EE ¹	EE ²	TDM	EE ¹	EE ²	TDM	EE	TDM	EE	TDM
1 ^a	8.20	8.19	0.646	8.42	8.41	0.295	8.17	0.643	8.43	0.654
2 ^b	9.33	9.32	0.518	9.56	9.55	0.258	9.31	0.522	9.57	0.521
3 ^c	9.72	9.71	0.088	9.97	9.96	0.040	9.70	0.047	9.92	0.120
4 ^d	10.44	10.43	0.901	10.69	10.68	0.469	10.42	0.892	10.40	0.704

¹ Uncorrected excitation energy.

² Corrected excitation energy.

^a $5p^5(^2P_{3/2})6s^2[3/2]_1^o$

^b $5p^5(^2P_{1/2})6s^2[1/2]_1^o$

^c $5p^5(^2P_{3/2})5d^2[1/2]_1^o$

^d $5p^5(^2P_{3/2})5d^2[3/2]_1^o$

3.3 Electron Attachment

3.3.1 Choice of truncation threshold

Figure 5 presents the convergence behavior of the absolute error in the computed electron affinity (EA) of the IBr molecule as a function of the truncation threshold in the SS-FNS and FNS truncation schemes, using the CD-based X2CAMF implementation of EA-ADC(3) with the s-aug-dyall.v2z basis set. The FNS approach shows a relatively slow and nonuniform convergence pattern, with large deviations (up to 3.5 eV) at lower truncation thresholds. In the FNS scheme, the diffuse orbitals are discarded during the truncation because they make a negligible contribution to the ground-state correlation energy. However, these diffuse functions are essential for the electron affinity problem, and discarding them is responsible for the slow convergence of EA values in the FNS-EA-ADC(3) method. In contrast, both the uncorrected and corrected SS-FNS schemes exhibit much faster and smoother convergence toward the canonical result. Even at the threshold of 10^{-3} , the SS-FNS methods show errors below 0.05 eV. The corrected SS-FNS variant further improves the results, and the result converges beyond 10^{-4} . These results demonstrate that the SS-FNS framework is reliable for truncating virtual space in electron affinity calculations. For further calculations in this section, we have employed a truncation threshold of $10^{-4.5}$.

3.3.2 Coin-age metal atoms

To access the performance of relativistic ADC(3) employing the SOC-X2CAMF Hamiltonian for the electron affinity problem, we have tested the SS-FNS-EA-ADC(3) and the corresponding semi-empirically scaled variant SS-FNS-EA-ADC[(2)+x(3)] for both atomic and molecular systems. For the atomic system, we have considered coinage metals Cu, Ag, and Au. Table 6 presents the calculated electron affinities (EAs) of the coinage metals Cu, Ag, and Au using different variants of the electron-attachment algebraic diagrammatic construction methods. Specifically, results from the CD-SOCX2CAMF-SS-FNS-EA-ADC(3) and

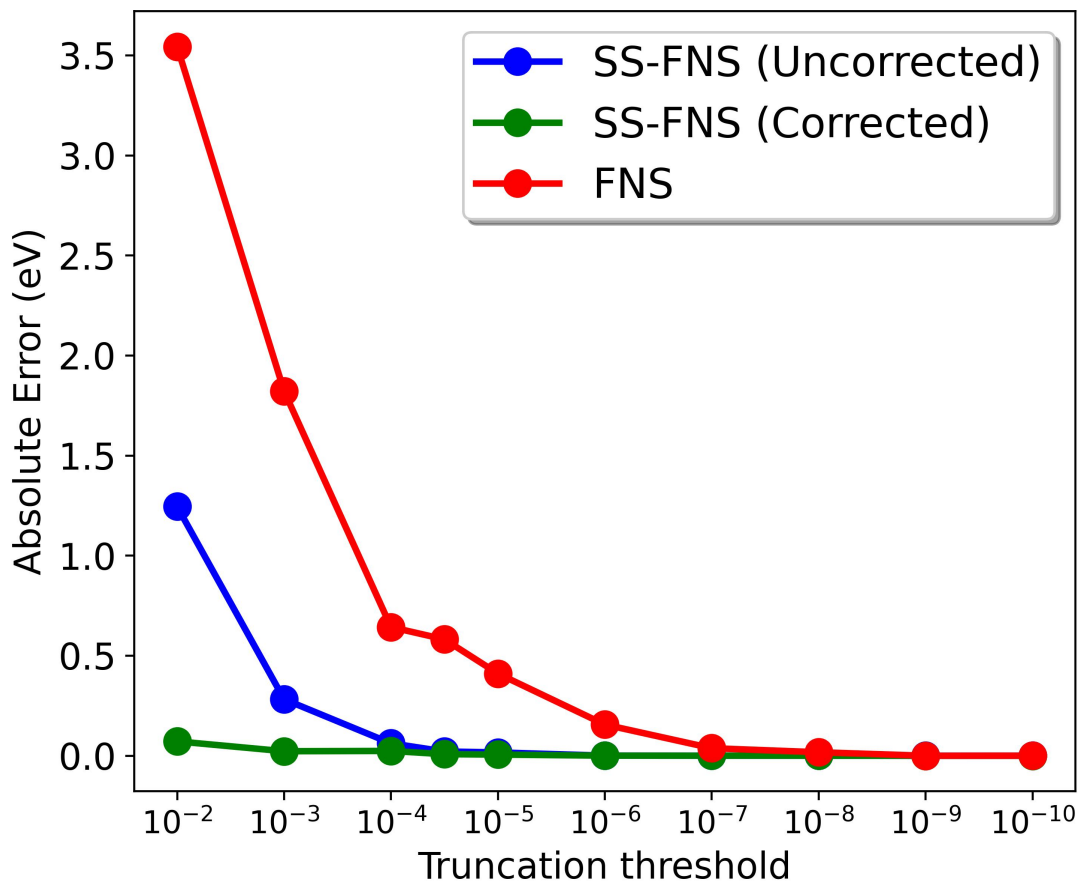


Figure 5: The comparison of absolute error in EA (in eV) for SS-FNS and FNS truncation schemes of CD-based X2CAMF version of EA-ADC(3) with respect to the canonical result for IBr molecule using s-aug-dyall.v2z at different truncation thresholds.

EA-ADC[(2)+x(3)] ($x = 0.5$) approaches are compared against canonical EA-ADC(3) and available experimental values. All calculations employed the d-aug-dyall.v4z basis set and the SOC-X2CAMF Hamiltonian, with the SS-FNS threshold set of $10^{-4.5}$. The canonical EA-ADC(3) method gives an EA value of 1.45 eV. For the SS-FNS-EA-ADC(3), the uncorrected and corrected electron affinities of Cu are 1.39 and 1.45 eV, respectively, indicating a modest but systematic improvement upon applying the perturbative correction. However, the SS-FNS-ADC(3) method shows an error of 0.21 eV with respect to the experiments for Cu. For Ag, the SS-FNS-EA-ADC(3) method shows improved performance, and the error with respect to the experiment is 0.04 eV. In contrast, the deviation from the canonical

Table 6: EAs of coinage metals using CD-SOCX2CAMF-SS-FNS variant of EA-ADC(3) and EA-ADC[(2)+x(3)] with d-aug-dyall.v4z and x=0.5. The canonical EA-ADC(3) calculations are also performed employing CD and SOC-X2CAMF Hamiltonian with d-aug-dyall.v4z basis set. All values are in eV.

System	SS-FNS-EA-ADC(3) ^a		SS-FNS-EA-ADC[(2)+x(3)] ^a		EA-ADC(3)	Expt
	Uncorrected	Corrected	Uncorrected	Corrected	Canonical	
Cu	1.39	1.45	1.13	1.20	1.45	1.23[104]
Ag	1.21	1.26	1.25	1.30	1.27	1.30[104]
Au	2.08	2.13	2.27	2.32	2.15	2.31[105]

^a With $10^{-4.5}$ FNS threshold.

EA-ADC(3) result is minimal—only about 0.01 eV. In the case of Au, both the uncorrected and corrected values slightly underestimate the experimental reference and show errors of 0.23 eV and 0.18 eV, respectively. In all the cases, the results are in excellent agreement with the corresponding canonical ADC(3) results. This SS-FNS-EA-ADC[(2)+x(3)] method is in excellent agreement with the experimental value, with a maximum deviation of 0.03 eV.

Table 7: EAs of silver monohalides AgX (X = Cl, Br, I) and AuCl using CD-SOCX2CAMF-SS-FNS variant of EA-ADC(3) and EA-ADC[(2)+x(3)] with s-aug-dyall.v4z and x=0.5. Experimental values are obtained from Ref.[106]. All values are in eV

System	SS-FNS-EA-ADC(3) ^a		SS-FNS-EA-ADC[(2)+x(3)] ^a		Expt
	Uncorrected	Corrected	Uncorrected	Corrected	
AgCl	1.40	1.45	1.46	1.51	1.59
AgBr	1.42	1.48	1.50	1.56	1.62
AgI	1.44	1.48	1.53	1.58	1.60
AuCl	1.94	1.98	2.05	2.09	2.22

^a With $10^{-4.5}$ FNS threshold.

3.3.3 Silver monohalides and AuCl

For the molecular system, we have chosen silver monohalides AgX (X = Cl, Br and I) and AuCl. Table 7 reports the calculated electron affinities (EAs) of the silver halides (AgCl,

AgBr, AgI) and gold chloride (AuCl) obtained using the CD-SOCX2CAMF-SS-FNS variants of EA-ADC(3) and EA-ADC[(2)+x(3)] ($x = 0.5$) with the s-aug-dyall.v4z basis set with an SS-FNS threshold of $10^{-4.5}$. Experimental reference values were taken from the photoelectron spectroscopy measurements of Wu et al.[106]. For the AgX series, both SS-FNS-EA-ADC(3) and SS-FNS-EA-ADC[(2)+x(3)] methods give good agreement with experimental electron affinities with excellent accuracy, though systematic differences between the two methods are evident. The corrected SS-FNS-EA-ADC(3) values are consistently lower than the corresponding SS-FNS-EA-ADC[(2)+x(3)] results by approximately 0.05–0.07 eV across the series. This upward shift introduced by the scaled third-order contribution in EA-ADC[(2)+x(3)] brings the results into closer agreement with experiment. For three AgX systems, SS-FNS-EA-ADC(3) shows a consistent underestimation of approximately 0.14 eV, which is reduced to less than 0.1 eV when moving to the ADC[(2)+x(3)] variant. For AuCl, the difference between the two approaches follows a similar trend. The corrected SS-FNS-EA-ADC(3) value of 1.98 eV slightly underestimates the experimental electron affinity (2.22 eV), while the EA-ADC[(2)+x(3)] result (2.09 eV) narrows this deviation to less than 0.15 eV. The larger electron affinity of AuCl relative to AgCl primarily arises from the stronger relativistic stabilization of the 6s orbital in Au, which enhances the electron binding energy. It is noteworthy that for both atomic and molecular systems, the CD-SOCX2CAMF-SS-FNS-EA-ADC[(2)+x(3)] methodology yields quantitatively more accurate electron affinities of heavy-element containing systems compared to the standard EA-ADC(3) approach.

3.4 Computational Efficiency

To evaluate the computational efficiency of the developed relativistic ADC(3) framework, wall-clock times were recorded for ionization potential (IP), electron attachment (EA), and electronic excitation (EE) calculations of the IBr molecule. All computations were performed on a single node equipped with an Intel(R) Xeon(R) Gold 5315Y CPU (3.20 GHz, 16 threads, x86_64 architecture) and 512 GB of RAM, running under identical numerical and convergence

settings. The SOC-X2CAMF Hamiltonian and the s-aug-dyall.v2z basis set were employed consistently. Canonical as well as FNS (for IP) and SS-FNS (for EA and EE) formulations were executed within the CD-SOCX2CAMF-ADC(3) implementation. As shown in Figure 6, the FNS/SS-FNS approaches offer a remarkable reduction in computational cost compared to their canonical counterparts. For the IP-ADC(3) calculation, the FNS formulation achieves nearly a sixfold speedup, reducing the total wall time from approximately 23 minutes to under 4 minutes. The improvement becomes even more pronounced for the EA-ADC(3) and EE-ADC(3) methods, where the SS-FNS variant shortens the computational time by factors of approximately 15 and 10, respectively. This efficiency gain originates primarily from the subspace-restricted integral transformation and reduced tensor contractions inherent to the FNS/SS-FNS schemes, which avoid the explicit construction of large canonical intermediates while maintaining accuracy. Overall, these results demonstrate that the FNS and SS-FNS formulations significantly enhance the scalability and practical feasibility of high-level relativistic ADC(3) methods for large-scale electron detachment, attachment, and excitation problems, without compromising the accuracy inherent in the theoretically rigorous canonical formalism.

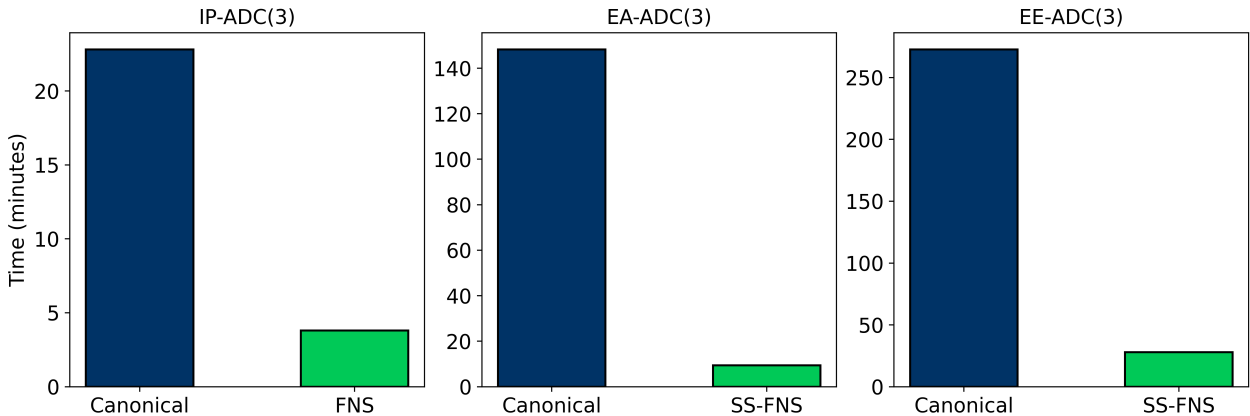


Figure 6: Total wall time taken for IP, EA, and EE-ADC(3) method for IBr molecule in canonical and FNS (for IP) or SS-FNS (for EA and EE) basis using s-aug-dyall.v2z basis set. Both canonical and FNS/SS-FNS calculations are performed using the SOC-X2CAMF Hamiltonian and employing CD.

3.5 Application to medium and large systems

To assess the efficiency of our newly developed approaches, FNS-CD-IP-ADC(3) and SS-FNS-CD-EE-ADC(3), we performed benchmark studies on medium- and large-sized systems. For the ionization potential (IP) case, two representative examples were chosen: (i) the hydrated anion $[\text{I}(\text{H}_2\text{O})_{12}]^-$, and (ii) a three-coordinate pincer-ligated $d^8\text{-Ir}(\text{tBu}^4\text{PGeCGeP})$ complex, where the central carbon belongs to a 2,6-disubstituted phenyl ring (Figure 7).

The structure of $[\text{I}(\text{H}_2\text{O})_{12}]^-$ complex was optimized using DFT at the B3LYP level, including scalar relativistic effects via the zero-order regular approximation (ZORA), as implemented in ORCA 6.0. The SARC-ZORA-TZVP basis set was employed for iodine, while the def2-TZVP basis was used for hydrogen and oxygen. For subsequent FNS-CD-IP-ADC(3) calculations, we used an uncontracted aug-cc-pVDZ basis set for H and O atoms and the s-aug-dyall.v4z basis for I. This results in a total of 1698 virtual spinors. The use of the FNS approximation leads to 114 occupied and 648 virtual spinors, and an auxiliary basis set dimension of 2,574 Cholesky. All computations were carried out sequentially on a workstation with dual Intel(R) Xeon(R) Gold 5315Y processors (3.20 GHz) and 2.0 TB of RAM. The formation of Cholesky vectors in the AO basis took 23 minutes 29 seconds, and the construction of FNS-based two-electron integrals required 1 hour 16 minutes 33 seconds. The ADC(3) step for computing the four lowest vertical IPs consumed 1 day 9 hours 45 minutes 50 seconds, yielding a total wall time of 1 day 16 hours 33 minutes 53 seconds. For comparison, the corresponding FNS-CD-IP-EOM-CCSD calculation required a significantly longer wall time of 4 days 19 hours 5 minutes[101]. The first vertical IP obtained from FNS-CD-IP-ADC(3) was 4.22 eV, while FNS-CD-IP-EOM-CCSD gave 4.30 eV. This demonstrates that the ADC(3)-based framework achieves a nearly threefold reduction in computational cost in comparison to an EOM-CCSD-based framework.

To test further with a larger system we have chosen a three-coordinate pincer-ligated $d^8\text{-Ir}(\text{tBu}^4\text{PGeCGeP})$ complex, where the central carbon belongs to a 2,6-disubstituted phenyl ring and it has relevance many areas of modern transition metal chemistry.[107, 108]

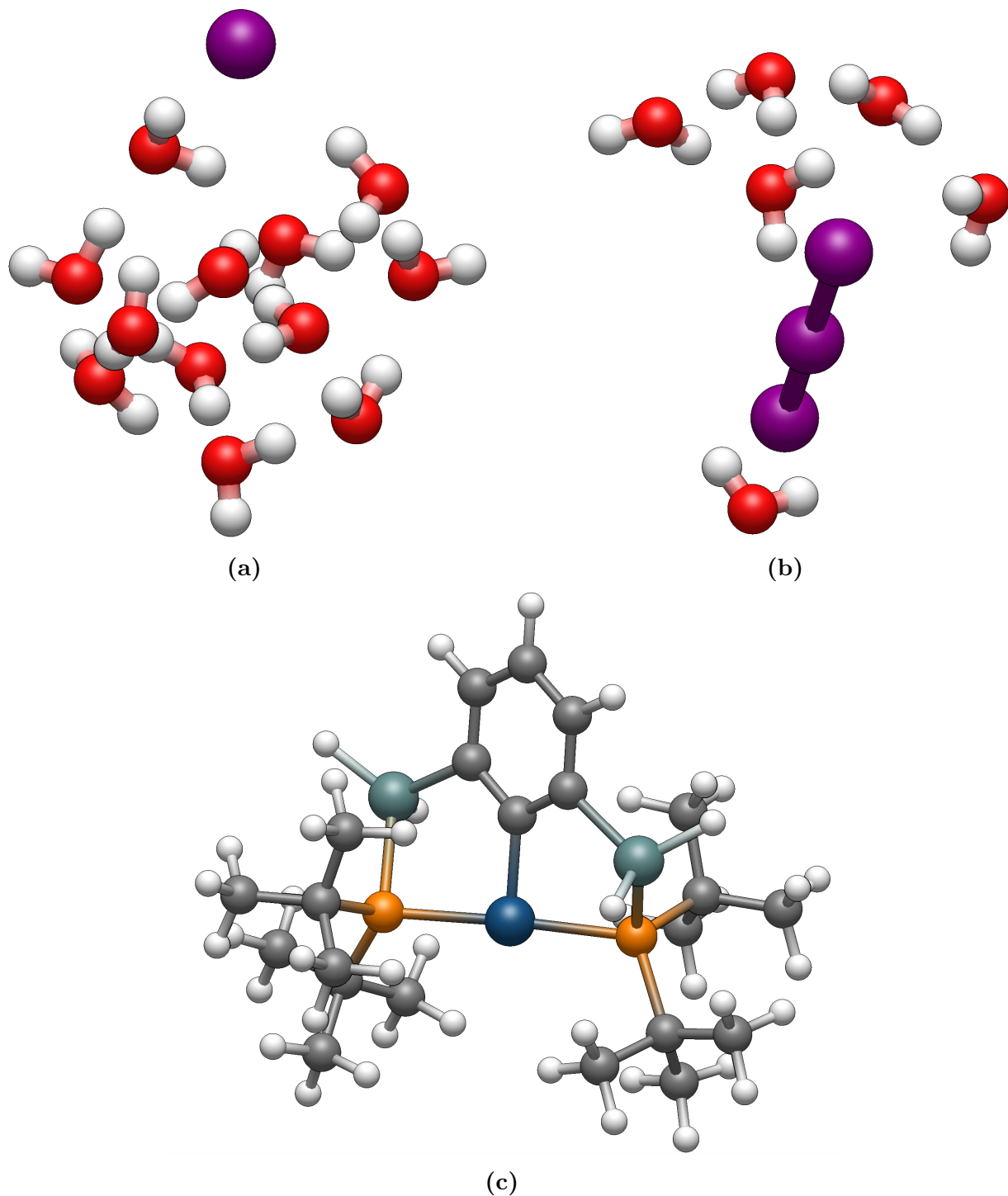


Figure 7: (a) $[\text{I}(\text{H}_2\text{O})_{12}]^-$ complex, (b) $[\text{I}_3(\text{H}_2\text{O})_6]^-$ complex, (c) Three-coordinated Pincer-Ligated $d^8\text{-Ir}(\text{tBu}_4\text{PGeCGeP})$ complex where C is a 2,6-disubstituted phenyl ring

As tridentate chelates, pincer ligands offer several channels to tune the electronic and steric environments of unsaturated metal fragments of relevance to catalysis.[109] In the present work, we have used FNS-CD-IP-ADC(3) to calculate IP of $\text{Ir}(\text{R}^4\text{PXCXP})$ complex, where R is a t-butyl group and X corresponds to a GeH_2 fragment, which acts as a linker. The $\text{Ir}(\text{R}^4\text{PXCXP})$ complex possesses a C_2 equilibrium geometry and the co-ordinates used for the present FNS-CD-IP-ADC(3) calculation have been taken from Ref. [110] We have used dyall.v2z basis set for Ir, Ge, and P, and uncontracted cc-pVDZ basis set for C and H, resulting in a total of 2650 basis functions with 346 occupied and 2304 virtual spinors. For the FNS-CD-IP-ADC(3) calculation, we have frozen 180 electrons and correlated 166 electrons. After employing FNS threshold of 10^{-4} and cholesky decomposition threshold of 10^{-3} , resulting in 4120 Cholesky vectors, 166 occupied and 1018 virtual spinors. With this correlation space, the time taken in solving only the ADC(3) secular equation using Davidson is 4 days, 54 minutes, and 56 seconds for calculating one IP state. The value obtained for the first IP of $\text{Ir}(\text{R}^4\text{PXCXP})$ complex is 6.76 eV, resulting from the removal of an electron from the valence d_{22} -type MO with a 2A symmetry.

For showcasing the performance of our SS-FNS-EE-ADC(3) implementation, we have considered $[\text{I}_3(\text{H}_2\text{O})_6]^-$ complex, and the excitation energy corresponding to the lowest excited state has been calculated. The geometry of the hexa-aqua triiodide complex has been obtained from Ref.[57] where they have used the same system for demonstrating the performance of the SS-FNS-EE-EOM-CCSD method. The dyall.av3z basis set has been used for the I atoms, and the uncontracted version of the cc-pVDZ basis set has been used for the O and H atoms. The hexa-aqua triiodide complex consists of 21 atoms with 220 electrons. The aforementioned basis set utilizes 1394 virtual spinors on a canonical basis, and a Cholesky threshold of 10^{-3} has been employed, resulting in 2580 Cholesky vectors. The SS-FNS-EE-ADC(3) calculation has been performed in a dedicated workstation with two Intel(R) Xeon(R) Gold 5315Y CPUs @ 3.20 GHz and 2 TB of total RAM. After applying frozen core approximation and using an FNS threshold of $10^{-4.5}$, the correlation space in

the truncated basis contains 70 occupied and 517 virtual spinors. The total time taken for this calculation is 3 days, 18 hours, 25 minutes, and 14 seconds, whereas with a similar computational setting, the SS-FNS-EE-EOM-CCSD took 5 days, 1 hour, 41 minutes. The total time taken in the ADC(3) part in the truncated basis is 2 days, 8 hours, 40 minutes, compared to 3 days, 16 hours, 32 minutes taken by the EOM-CCSD version. The excitation energy obtained for this complex of the 2_g state is 2.16 eV.

4 Conclusion

In this work, we have developed a low-cost relativistic third-order ADC framework using Cholesky decomposition, frozen natural spinors, and the exact two-component atomic mean-field Hamiltonian to compute ionization, electron affinity, and excitation properties of heavy-element systems. The inclusion of state-specific frozen natural spinors ensures accurate treatment of excited states, while the CD approach drastically reduces memory and storage requirements. Across diverse benchmarks—ranging from ionization potentials of the SOC-81 set to fine-structure splittings in halogen oxides, photoelectron spectra of cadmium halides, and excitation energies of Ga^+ , In^+ , Tl^+ , $\text{I}3^-$, Xe the method consistently reproduces canonical reference results with high accuracy. Importantly, the approach captures spin-orbit coupling effects without prohibitive computational cost, enabling reliable calculations in systems previously inaccessible to canonical four-component ADC(3). Furthermore, owing to the perturbative ground-state treatment and Hermitian formulation of the ADC framework, we are able to compute excitation energies and transition properties for a wide variety of excited states at significantly lower computational cost compared to EOM-CCSD. With the present implementation, we have also successfully calculated the ionization potential of a three-coordinated pincer-ligated complex comprising more than 2600 basis functions, where even after truncation, the virtual space dimension exceeded 1000. These results clearly demonstrate both the efficiency and robustness of the relativistic ADC(3) implementation

in tackling large-scale systems. The obtained results show that the accuracy of the standard relativistic ADC(3) method is inferior to the EOM-CCSD method at the same level of truncation for IP, EA, and excitation energy. The use of the matrix scaling method can improve the accuracy of ADC(3) methods in certain cases. However, their performance is not always consistent. Therefore, it is necessary to develop more accurate approximations within the ADC framework. Work is in progress in that direction.

5 Acknowledgment

AKD, SC, and KM acknowledge the support from IIT Bombay. DST-SERB, CSIR-India, DST-Inspire Faculty Fellowship, and ISRO for financial support. The authors also acknowledge the IIT Bombay supercomputing facility and C-DAC (Param Smriti and Param Bramha) for providing computational resources. SC acknowledges the Prime Minister’s Research Fellowship (PMRF), and KM acknowledges CSIR-HRDG for the research fellowship. AKD acknowledges the research fellowship funded by the EU NextGenerationEU through the Recovery and Resilience Plan for Slovakia under project No. 09I03-03-V04-00117.

References

- (1) González, L.; Lindh, R. *Quantum chemistry and dynamics of excited states: methods and applications*; John Wiley & Sons, 2020.
- (2) Krylov, A. I. Equation-of-motion coupled-cluster methods for open-shell and electronically excited species: The hitchhiker’s guide to Fock space. *Annu. Rev. Phys. Chem.* **2008**, *59*, 433–462.
- (3) Nooijen, M.; Snijders, J. G. Coupled cluster approach to the single-particle Green’s function. *International Journal of Quantum Chemistry* **1992**, *44*, 55–83.

- (4) Stanton, J. F.; Bartlett, R. J. The equation of motion coupled-cluster method. A systematic biorthogonal approach to molecular excitation energies, transition probabilities, and excited state properties. *The Journal of chemical physics* **1993**, *98*, 7029–7039.
- (5) Rowe, D. Equations-of-motion method and the extended shell model. *Reviews of Modern Physics* **1968**, *40*, 153.
- (6) Koch, H.; Jensen, H. J.; Jorgensen, P.; Helgaker, T. Excitation energies from the coupled cluster singles and doubles linear response function (CCSDLR). Applications to Be, CH sup+, CO, and H sub 2 O. *Journal of Chemical Physics;(USA)* **1990**, *93*.
- (7) Sekino, H.; Bartlett, R. J. A linear response, coupled-cluster theory for excitation energy. *International Journal of Quantum Chemistry* **1984**, *26*, 255–265.
- (8) Thomas, S.; Hampe, F.; Stopkowicz, S.; Gauss, J. Complex ground-state and excitation energies in coupled-cluster theory. *Molecular Physics* **2021**, *119*, e1968056.
- (9) Liu, J.; Asthana, A.; Cheng, L.; Mukherjee, D. Unitary coupled-cluster based self-consistent polarization propagator theory: A third-order formulation and pilot applications. *The Journal of chemical physics* **2018**, *148*.
- (10) Liu, J.; Cheng, L. Unitary coupled-cluster based self-consistent polarization propagator theory: A quadratic unitary coupled-cluster singles and doubles scheme. *The Journal of Chemical Physics* **2021**, *155*.
- (11) Majee, K.; Chakraborty, S.; Mukhopadhyay, T.; Nayak, M. K.; Dutta, A. K. A reduced cost four-component relativistic unitary coupled cluster method for atoms and molecules. *The Journal of Chemical Physics* **2024**, *161*.
- (12) Majee, K.; Chamoli, S.; Nayak, M. K.; Dutta, A. K. Relativistic unitary coupled

- cluster method for ground-state molecular properties. *arXiv preprint arXiv:2510.18709* **2025**,
- (13) Schirmer, J.; Trofimov, A. B. Intermediate state representation approach to physical properties of electronically excited molecules. *The Journal of chemical physics* **2004**, *120*, 11449–11464.
- (14) Mertins, F.; Schirmer, J. Algebraic propagator approaches and intermediate-state representations. I. The biorthogonal and unitary coupled-cluster methods. *Physical Review A* **1996**, *53*, 2140.
- (15) Schirmer, J. Closed-form intermediate representations of many-body propagators and resolvent matrices. *Physical Review A* **1991**, *43*, 4647.
- (16) Schirmer, J. Beyond the random-phase approximation: A new approximation scheme for the polarization propagator. *Physical Review A* **1982**, *26*, 2395.
- (17) von Niessen, W.; Schirmer, J.; Cederbaum, L. S. Computational methods for the one-particle green's function. *Computer Physics Reports* **1984**, *1*, 57–125.
- (18) Dreuw, A.; Wormit, M. The algebraic diagrammatic construction scheme for the polarization propagator for the calculation of excited states. *Wiley Interdisciplinary Reviews: Computational Molecular Science* **2015**, *5*, 82–95.
- (19) Dempwolff, A. L.; Schneider, M.; Hodecker, M.; Dreuw, A. Efficient implementation of the non-Dyson third-order algebraic diagrammatic construction approximation for the electron propagator for closed-and open-shell molecules. *The Journal of Chemical Physics* **2019**, *150*.
- (20) Trofimov, A.; Stelter, G.; Schirmer, J. A consistent third-order propagator method for electronic excitation. *The Journal of Chemical Physics* **1999**, *111*, 9982–9999.

- (21) Fetter, A. L.; Walecka, J. D. *Quantum theory of many-particle systems*; Courier Corporation, 2012.
- (22) Cederbaum, L. One-body Green's function for atoms and molecules: theory and application. *Journal of Physics B: Atomic and Molecular Physics* **1975**, *8*, 290.
- (23) Cederbaum, L.; Domcke, W. Theoretical aspects of ionization potentials and photoelectron spectroscopy: a Green's function approach. *Advances in chemical physics* **1977**, *36*, 205–344.
- (24) Schirmer, J.; Cederbaum, L. The two-particle-hole Tamm-Dancoff approximation (2ph-TDA) equations for closed-shell atoms and molecules. *Journal of Physics B: Atomic and Molecular Physics* **1978**, *11*, 1889.
- (25) Leitner, J.; Dempwolff, A.; Dreuw, A. The fourth-order algebraic diagrammatic construction scheme for the polarization propagator. *The Journal of chemical physics* **2022**, *157*.
- (26) Leitner, J.; Dempwolff, A. L.; Dreuw, A. Fourth-order algebraic diagrammatic construction for electron detachment and attachment: The IP-and EA-ADC (4) methods. *The Journal of Physical Chemistry A* **2024**, *128*, 7680–7690.
- (27) Schirmer, J.; Cederbaum, L. S.; Walter, O. New approach to the one-particle Green's function for finite Fermi systems. *Physical Review A* **1983**, *28*, 1237.
- (28) Angonoa, G.; Walter, O.; Schirmer, J. Theoretical K-shell ionization spectra of N₂ and CO by a fourth-order Green's function method. *The Journal of Chemical Physics* **1987**, *87*, 6789–6801.
- (29) Trofimov, A. B.; Schirmer, J. An efficient polarization propagator approach to valence electron excitation spectra. *Journal of Physics B: Atomic, Molecular and Optical Physics* **1995**, *28*, 2299.

- (30) Trofimov, A.; Schirmer, J. Polarization propagator study of electronic excitation in key heterocyclic molecules I. Pyrrole. *Chemical physics* **1997**, *214*, 153–170.
- (31) Trofimov, A.; Schirmer, J. Molecular ionization energies and ground-and ionic-state properties using a non-Dyson electron propagator approach. *The Journal of chemical physics* **2005**, *123*.
- (32) Dylla, K. G.; Fægri, K. *Introduction to relativistic quantum chemistry*; Oxford University Press, 2007.
- (33) Pernpointner, M. The relativistic polarization propagator for the calculation of electronic excitations in heavy systems. *The Journal of Chemical Physics* **2014**, *140*.
- (34) Pernpointner, M.; Visscher, L.; Trofimov, A. B. Four-component polarization propagator calculations of electron excitations: Spectroscopic implications of spin–orbit coupling effects. *Journal of Chemical Theory and Computation* **2018**, *14*, 1510–1522.
- (35) Pernpointner, M.; Trofimov, A. The one-particle Green’s function method in the Dirac–Hartree–Fock framework. I. Second-order valence ionization energies of Ne through Xe. *The Journal of chemical physics* **2004**, *120*, 4098–4106.
- (36) Pernpointner, M. The four-component two-particle propagator for the calculation of double-ionization spectra of heavy-element compounds: I. Method. *Journal of Physics B: Atomic, Molecular and Optical Physics* **2010**, *43*, 205102.
- (37) Pernpointner, M. The effect of the Gaunt interaction on the molecular ionization spectra of CO, H₂S and TH. *Journal of Physics B: Atomic, Molecular and Optical Physics* **2005**, *38*, 1955.
- (38) Chakraborty, S.; Mukhopadhyay, T.; Nayak, M. K.; Dutta, A. K. A relativistic third-order algebraic diagrammatic construction theory for electron detachment, attachment, and excitation problems. *The Journal of Chemical Physics* **2025**, *162*.

- (39) Hess, B. A. Relativistic electronic-structure calculations employing a two-component no-pair formalism with external-field projection operators. *Physical Review A* **1986**, *33*, 3742.
- (40) van Lenthe, E.; Van Leeuwen, R.; Baerends, E.; Snijders, J. Relativistic regular two-component Hamiltonians. *International Journal of Quantum Chemistry* **1996**, *57*, 281–293.
- (41) Dyall, K. G. Interfacing relativistic and nonrelativistic methods. I. Normalized elimination of the small component in the modified Dirac equation. *The Journal of chemical physics* **1997**, *106*, 9618–9626.
- (42) Nakajima, T.; Hirao, K. A new relativistic theory: a relativistic scheme by eliminating small components (RESC). *Chemical physics letters* **1999**, *302*, 383–391.
- (43) Liu, W.; Peng, D. Exact two-component Hamiltonians revisited. *The Journal of chemical physics* **2009**, *131*.
- (44) Saue, T. Relativistic Hamiltonians for chemistry: A primer. *ChemPhysChem* **2011**, *12*, 3077–3094.
- (45) Liu, J.; Cheng, L. An atomic mean-field spin-orbit approach within exact two-component theory for a non-perturbative treatment of spin-orbit coupling. *The Journal of Chemical Physics* **2018**, *148*.
- (46) Zhang, C.; Cheng, L. Atomic mean-field approach within exact two-component theory based on the Dirac–Coulomb–Breit Hamiltonian. *The Journal of Physical Chemistry A* **2022**, *126*, 4537–4553.
- (47) Knecht, S.; Repisky, M.; Jensen, H. J. A.; Saue, T. Exact two-component Hamiltonians for relativistic quantum chemistry: Two-electron picture-change corrections made simple. *The Journal of Chemical Physics* **2022**, *157*.

- (48) Helmich-Paris, B.; Repisky, M.; Visscher, L. Relativistic Cholesky-decomposed density matrix MP2. *Chemical Physics* **2019**, *518*, 38–46.
- (49) Banerjee, S.; Zhang, T.; Dyall, K. G.; Li, X. Relativistic resolution-of-the-identity with Cholesky integral decomposition. *The Journal of Chemical Physics* **2023**, *159*.
- (50) Uhlirova, T.; Cianchino, D.; Nottoli, T.; Lipparini, F.; Gauss, J. Cholesky Decomposition in Spin-Free Dirac–Coulomb Coupled-Cluster Calculations. *The Journal of Physical Chemistry A* **2024**, *128*, 8292–8303.
- (51) Majumder, R.; Sokolov, A. Y. Algebraic Diagrammatic Construction Theory of Charged Excitations with Consistent Treatment of Spin–Orbit Coupling and Dynamic Correlation. *Journal of Chemical Theory and Computation* **2025**, *21*, 2414–2431, PMID: 39979128.
- (52) Pototschnig, J. V.; Papadopoulos, A.; Lyakh, D. I.; Repisky, M.; Halbert, L.; Severo Pereira Gomes, A.; Jensen, H. J. A.; Visscher, L. Implementation of relativistic coupled cluster theory for massively parallel GPU-accelerated computing architectures. *Journal of chemical theory and computation* **2021**, *17*, 5509–5529.
- (53) Chamoli, S.; Surjuse, K.; Jangid, B.; Nayak, M. K.; Dutta, A. K. A reduced cost four-component relativistic coupled cluster method based on natural spinors. *The Journal of Chemical Physics* **2022**, *156*.
- (54) Surjuse, K.; Chamoli, S.; Nayak, M. K.; Dutta, A. K. A low-cost four-component relativistic equation of motion coupled cluster method based on frozen natural spinors: Theory, implementation, and benchmark. *The Journal of Chemical Physics* **2022**, *157*.
- (55) Yuan, X.; Visscher, L.; Gomes, A. S. P. Assessing MP2 frozen natural orbitals in relativistic correlated electronic structure calculations. *The Journal of Chemical Physics* **2022**, *156*.

- (56) Chamoli, S.; Wang, X.; Zhang, C.; Nayak, M. K.; Dutta, A. K. Frozen Natural Spinors for Cholesky Decomposition-Based Two-Component Relativistic Coupled Cluster Method. *Journal of Chemical Theory and Computation* **2025**, *21*, 4532–4542.
- (57) Mukhopadhyay, T.; Thapa, M.; Chamoli, S.; Wang, X.; Zhang, C.; Nayak, M. K.; Dutta, A. K. Reduced-cost relativistic equation-of-motion coupled cluster method based on frozen natural spinors: A state-specific approach. *The Journal of Chemical Physics* **2025**, *163*, 194107.
- (58) Schirmer, J. *Many-body methods for atoms, molecules and clusters*; Springer, 2018; Vol. 94.
- (59) Oddershede, J. *Advances in quantum chemistry*; Elsevier, 1978; Vol. 11; pp 275–352.
- (60) Oddershede, J.; Jørgensen, P.; Yeager, D. L. Polarization propagator methods in atomic and molecular calculations. *Computer Physics Reports* **1984**, *2*, 33–92.
- (61) Oddershede, J. Propagator methods. *Adv. Chem. Phys* **1987**, *69*, 201–239.
- (62) Ortiz, J. V. Electron propagator theory: an approach to prediction and interpretation in quantum chemistry. *Wiley Interdisciplinary Reviews: Computational Molecular Science* **2013**, *3*, 123–142.
- (63) Trofimov, A.; Schirmer, J. Polarization propagator study of electronic excitation in key heterocyclic molecules II. Furan. *Chemical physics* **1997**, *224*, 175–190.
- (64) Schirmer, J.; Angonoa, G. On Green’s function calculations of the static self-energy part, the ground state energy and expectation values. *The Journal of chemical physics* **1989**, *91*, 1754–1761.
- (65) Schirmer, J.; Trofimov, A.; Stelter, G. A non-Dyson third-order approximation scheme for the electron propagator. *The Journal of chemical physics* **1998**, *109*, 4734–4744.

- (66) Mertins, F.; Schirmer, J.; Tarantelli, A. Algebraic propagator approaches and intermediate-state representations. II. The equation-of-motion methods for N , $N\pm 1$, and $N\pm 2$ electrons. *Physical Review A* **1996**, *53*, 2153.
- (67) Bauer, M.; Dempwolff, A. L.; Rehn, D. R.; Dreuw, A. Exploring the Accuracy and Usefulness of Semi-Empirically Scaled ADC Schemes by Blending Second and Third Order Terms. *J. Chem. Phys.* **2022**, *156*, 144101.
- (68) Mukhopadhyay, T.; Majee, K.; Dutta, A. K. A reduced-cost third-order algebraic diagrammatic construction based on state-specific frozen natural orbitals: Application to the electron-attachment problem. *arXiv preprint arXiv:2511.05897* **2025**,
- (69) Dyall, K. G. An Exact Separation of the Spin-free and Spin-dependent Terms of the Dirac–Coulomb–Breit Hamiltonian. *The Journal of Chemical Physics* **1994**, *100*, 2118–2127.
- (70) Heß, B. A.; Marian, C. M.; Wahlgren, U.; Gropen, O. A Mean-Field Spin-Orbit Method Applicable to Correlated Wavefunctions. *Chemical Physics Letters* **1996**, *251*, 365–371.
- (71) Liu, J.; Cheng, L. An Atomic Mean-Field Spin-Orbit Approach within Exact Two-Component Theory for a Non-Perturbative Treatment of Spin-Orbit Coupling. *The Journal of Chemical Physics* **2018**, *148*, 144108.
- (72) Knecht, S.; Repisky, M.; Jensen, H. J. A.; Saue, T. Exact Two-Component Hamiltonians for Relativistic Quantum Chemistry: Two-electron Picture-Change Corrections Made Simple. *The Journal of Chemical Physics* **2022**, *157*, 114106.
- (73) Zhang, C.; Cheng, L. Atomic Mean-Field Approach within Exact Two-Component Theory Based on the Dirac–Coulomb–Breit Hamiltonian. *The Journal of Physical Chemistry A* **2022**, *126*, 4537–4553.

- (74) Hättig, C. In *Advances in Quantum Chemistry*; Jensen, H. J. Å., Ed.; Response Theory and Molecular Properties (A Tribute to Jan Linderberg and Poul Jørgensen); Academic Press, 2005; Vol. 50; pp 37–60.
- (75) Hohenstein, E. G.; Sherrill, C. D. Density Fitting and Cholesky Decomposition Approximations in Symmetry-Adapted Perturbation Theory: Implementation and Application to Probe the Nature of π - π Interactions in Linear Acenes. *The Journal of Chemical Physics* **2010**, *132*, 184111.
- (76) Aquilante, F.; Boman, L.; Boström, J.; Koch, H.; Lindh, R.; de Merás, A. S.; Pedersen, T. B. *Linear-Scaling Techniques in Computational Chemistry and Physics: Methods and Applications*; Springer, 2011; pp 301–343.
- (77) Folkestad, S. D.; Kjønstad, E. F.; Koch, H. An efficient algorithm for Cholesky decomposition of electron repulsion integrals. *The Journal of chemical physics* **2019**, *150*.
- (78) Zhang, T.; Liu, X.; Valeev, E. F.; Li, X. Toward the minimal floating operation count Cholesky decomposition of electron repulsion integrals. *The Journal of Physical Chemistry A* **2021**, *125*, 4258–4265.
- (79) Chamoli, S.; Surjuse, K.; Jangid, B.; Nayak, M. K.; Dutta, A. K. A Reduced Cost Four-Component Relativistic Coupled Cluster Method Based on Natural Spinors. *The Journal of Chemical Physics* **2022**, *156*, 204120.
- (80) Yuan, X.; Visscher, L.; Gomes, A. S. P. Assessing MP2 Frozen Natural Orbitals in Relativistic Correlated Electronic Structure Calculations. *The Journal of Chemical Physics* **2022**, *156*, 224108.
- (81) Majee, K.; Chakraborty, S.; Mukhopadhyay, T.; Nayak, M. K.; Dutta, A. K. A Reduced Cost Four-Component Relativistic Unitary Coupled Cluster Method for Atoms and Molecules. *The Journal of Chemical Physics* **2024**, *161*, 034101.

- (82) Chakraborty, S.; Manna, A.; Crawford, T. D.; Dutta, A. K. A Low-Cost Four-Component Relativistic Coupled Cluster Linear Response Theory Based on Perturbation Sensitive Natural Spinors. *J. Chem. Phys.* **2025**, *163*, 044111.
- (83) Löwdin, P.-O. Quantum Theory of Many-Particle Systems. I. Physical Interpretations by Means of Density Matrices, Natural Spin-Orbitals, and Convergence Problems in the Method of Configurational Interaction. *Physical Review* **1955**, *97*, 1474–1489.
- (84) Chamoli, S.; Nayak, M. K.; Dutta, A. K. *Electron Density*; John Wiley & Sons, Ltd, 2024; Chapter 5, pp 83–96.
- (85) Chamoli, S.; Nayak, M. K.; Dutta, A. K. A Reduced Cost Two-Component Relativistic Equation-of-Motion Coupled Cluster Method for Ionization Potential. *Journal of Chemical Theory and Computation* **2025**, *21*, 8823–8832, PMID: 40947597.
- (86) Mandal, S.; Dutta, A. K. A Third-Order Relativistic Algebraic Diagrammatic Construction Method for Double Ionization Potentials: Theory, Implementation, and Benchmark. *arXiv preprint arXiv:2508.19012* **2025**,
- (87) Mukhopadhyay, T.; Mukherjee, M.; Gururangan, K.; Piecuch, P.; Dutta, A. K. Reduced-Cost Four-Component Relativistic Double Ionization Potential Equation-of-Motion Coupled-Cluster Approaches with 4-Hole–2-Particle Excitations and Three-Body Clusters. *arXiv preprint arXiv:2509.14779* **2025**,
- (88) Manna, A.; Dutta, A. K. A reduced cost equation of motion coupled cluster method for excited states based on state-specific natural orbitals: Theory, Implementation, Benchmark. 2025; <https://arxiv.org/abs/2506.16894>.
- (89) Pernpointner, M. The Relativistic Polarization Propagator for the Calculation of Electronic Excitations in Heavy Systems. *The Journal of Chemical Physics* **2014**, *140*, 084108.

- (90) Pernpointner, M.; Visscher, L.; Trofimov, A. B. Four-Component Polarization Propagator Calculations of Electron Excitations: Spectroscopic Implications of Spin–Orbit Coupling Effects. *Journal of Chemical Theory and Computation* **2018**, *14*, 1510–1522.
- (91) Hirao, K.; Nakatsuji, H. A Generalization of the Davidson’s Method to Large Nonsymmetric Eigenvalue Problems. *Journal of Computational Physics* **1982**, *45*, 246–254.
- (92) Mukhopadhyay, T.; Jangid, B.; Dutta, A. K. State-specific frozen natural orbital for reduced-cost algebraic diagrammatic construction calculations: The application to ionization problem. *The Journal of Chemical Physics* **2023**, *159*.
- (93) Manna, A.; Jangid, B.; Pant, R.; Dutta, A. K. Efficient State-Specific Natural Orbital Based Equation of Motion Coupled Cluster Method for Core-Ionization Energies: Theory, Implementation, and Benchmark. *Journal of Chemical Theory and Computation* **2024**, *20*, 6604–6620.
- (94) Dutta, A.; Manna, A.; Jangid, B.; Majee, K.; Surjuse, K.; Mukherjee, M.; Thapa, M.; Arora, S.; Chamoli, S.; Haldar, S.; Chakraborty, S.; Mandal, S.; Mukhopadhyay, T. BAGH: A quantum chemistry software package. **2025**,
- (95) Sun, Q. Libcint: An efficient general integral library for gaussian basis functions. *Journal of computational chemistry* **2015**, *36*, 1664–1671.
- (96) Sun, Q.; Berkelbach, T. C.; Blunt, N. S.; Booth, G. H.; Guo, S.; Li, Z.; Liu, J.; McClain, J. D.; Sayfutyarova, E. R.; Sharma, S.; others PySCF: the Python-based simulations of chemistry framework. *Wiley Interdisciplinary Reviews: Computational Molecular Science* **2018**, *8*, e1340.
- (97) Sun, Q.; Zhang, X.; Banerjee, S.; Bao, P.; Barbry, M.; Blunt, N. S.; Bogdanov, N. A.; Booth, G. H.; Chen, J.; Cui, Z.-H.; others Recent developments in the PySCF program package. *The Journal of chemical physics* **2020**, *153*.

- (98) Wang, X. socutils. <https://github.com/xubwa/socutils.git>, 2025; GitHub repository.
- (99) Bast, R.; Gomes, A.; Saue, T.; Visscher, L.; Jensen, H.; Aucar, I.; Bakken, V.; Chibueze, C.; Creutzberg, J.; Dyall, K.; others DIRAC23. *Zenodo* **2023**,
- (100) Barca, G. M.; Bertoni, C.; Carrington, L.; Datta, D.; De Silva, N.; Deustua, J. E.; Fedorov, D. G.; Gour, J. R.; Gunina, A. O.; Guidez, E.; others Recent developments in the general atomic and molecular electronic structure system. *The Journal of chemical physics* **2020**, *152*.
- (101) Chamoli, S.; Nayak, M. K.; Dutta, A. K. A Reduced Cost Two-Component Relativistic Equation-of-Motion Coupled Cluster Method for Ionization Potential. *Journal of Chemical Theory and Computation* **2025**,
- (102) Abraham, V.; Harsha, G.; Zgid, D. Relativistic fully self-consistent GW for molecules: Total energies and ionization potentials. *Journal of Chemical Theory and Computation* **2024**, *20*, 4579–4590.
- (103) Shee, A.; Saue, T.; Visscher, L.; Gomes, A. S. P. Equation-of-Motion Coupled-Cluster Theory Based on the 4-Component Dirac–Coulomb(–Gaunt) Hamiltonian. Energies for Single Electron Detachment, Attachment, and Electronically Excited States. *The Journal of Chemical Physics* **2018**, *149*, 174113.
- (104) Bilodeau, R. C.; Scheer, M.; Haugen, H. K. Infrared laser photodetachment of transition metal negative ions: studies on, and. *Journal of Physics B: Atomic, Molecular and Optical Physics* **1998**, *31*, 3885.
- (105) Gantefor, G.; Cox, D. M.; Kaldor, A. Zero electron kinetic energy spectroscopy of Au-6. *The Journal of chemical physics* **1992**, *96*, 4102–4105.

- (106) Wu, X.; Xie, H.; Qin, Z.; Tan, K.; Tang, Z.; Lu, X. Photoelectron Imaging and Theoretical Studies of Silver Monohalides AgX-(X= Cl, Br, I) and AuCl-. *The Journal of Physical Chemistry A* **2011**, *115*, 6321–6326.
- (107) van Koten, G. Pincer ligands as powerful tools for catalysis in organic synthesis. *Journal of Organometallic Chemistry* **2013**, *730*, 156–164.
- (108) Van Koten, G.; Milstein, D. *Organometallic pincer chemistry*; Springer, 2012; Vol. 40.
- (109) Roddick, D. M. *Organometallic Pincer Chemistry*; Springer, 2012; pp 49–88.
- (110) Baroudi, A.; El-Hellani, A.; Bengali, A. A.; Goldman, A. S.; Hasanayn, F. Calculation of ionization energy, electron affinity, and hydride affinity trends in pincer-ligated d8-Ir (tBu4PXCXP) complexes: Implications for the thermodynamics of oxidative H₂ addition. *Inorganic Chemistry* **2014**, *53*, 12348–12359.